

DOT/FAA/AR-01/57

Office of Aviation Research
Washington, D.C. 20591

Investigation of Adhesive Behavior in Aircraft Applications

September 2001

Final Report

This document is available to the U.S. public
through the National Technical Information
Service (NTIS), Springfield, Virginia 22161.



U.S. Department of Transportation
Federal Aviation Administration

DISTRIBUTION STATEMENT A
Approved for Public Release
Distribution Unlimited

20011214 094

NOTICE

This document is disseminated under the sponsorship of the U.S. Department of Transportation in the interest of information exchange. The United States Government assumes no liability for the contents or use thereof. The United States Government does not endorse products or manufacturers. Trade or manufacturer's names appear herein solely because they are considered essential to the objective of this report. This document does not constitute FAA certification policy. Consult your local FAA aircraft certification office as to its use.

This report is available at the Federal Aviation Administration William J. Hughes Technical Center's Full-Text Technical Reports page: actlibrary.tc.faa.gov in Adobe Acrobat portable document format (PDF).

1. Report No. DOT/FAA/AR-01/57	2. Government Accession No.	3. Recipient's Catalog No.	
4. Title and Subtitle INVESTIGATION OF ADHESIVE BEHAVIOR IN AIRCRAFT APPLICATIONS		5. Report Date September 2001	
		6. Performing Organization Code	
7. Author(s) Charles Yang and John S. Tomblin		8. Performing Organization Report No.	
9. Performing Organization Name and Address Department of Mechanical Engineering Wichita State University Wichita, KS 67260		10. Work Unit No. (TRAIS)	
		11. Contract or Grant No. IA031	
12. Sponsoring Agency Name and Address U.S. Department of Transportation Federal Aviation Administration Office of Aviation Research Washington, DC 20591		13. Type of Report and Period Covered Final Report	
		14. Sponsoring Agency Code ACE-110	
15. Supplementary Notes The FAA William J. Hughes Technical Center Technical Monitor was Peter Shyprykevich.			
16. Abstract There are two parts included in this report. The first part evaluates the most commonly used test method for adhesive properties, ADTM D 5656 "Standard Test Method for Thick-Adherend Metal Lap-Shear Joints for Determination of the Stress-Strain Behavior of Adhesives in Shear by Tension Loading." Finite element analyses were conducted to simulate the specimen behavior following the ASTM procedures. It was found that deviations of the measured adhesive shear modulus from the true value can be as large as 20% if corrections are not made. Correction factors based on different bondline thicknesses and adhesive properties are provided in the report. There are generally three failure modes of adhesive-bonded composite joints: (1) adherend failure, (2) adhesive failure of the adhesive, and (3) cohesive failure of the adhesive. The second part of this report provides (1) an analytical model for predicting stress distributions within an adhesive-bonded composite joint using ASTM D 3165 test specimen dimensions and (2) a method for predicting joint strength under the adherend failure mode. The analytical model was verified using a finite element model and comparing the adhesive stress distributions of the two analyses. A failure analysis was conducted based on four failure criteria. Predicted strengths were compared with test data. It was shown that the maximum interlaminar axial tensile stress criteria predict the joint strength better than Tsai-Hill and von Mises criteria.			
17. Key Words Composite joints, Adhesive joints, Adhesive property, ASTM D 1002, ASTM D 3165, ASTM D 5656.		18. Distribution Statement This document is available to the public through the National Technical Information Service (NTIS), Springfield, Virginia 22161.	
19. Security Classif. (of this report) Unclassified	20. Security Classif. (of this page) Unclassified	21. No. of Pages 52	22. Price

TABLE OF CONTENTS

	Page
EXECUTIVE SUMMARY	vii
1. EVALUATION AND ADJUSTMENT OF ASTM D 5656 "STANDARD TEST METHOD FOR THICK-ADHEREND METAL LAP-SHEAR JOINTS FOR DETERMINATION OF THE STRESS-STRAIN BEHAVIOR OF ADHESIVES IN SHEAR BY TENSION LOADING"	1
1.1 Introduction	1
1.2 ASTM D 5656 Measurement and Analysis	3
1.3 Sources of Error	5
1.4 Finite Element Analysis	6
1.5 Results and Discussion	7
2. STRESS MODEL AND INTERLAMINAR FAILURE OF ADHESIVE-BONDED COMPOSITE JOINTS USING ASTM D 3165 SPECIMENS	15
2.1 Introduction	15
2.2 Model Derivation	17
2.2.1 Adherend Formulation	17
2.2.2 Adhesive Formulation	20
2.2.3 Overall Governing Equations	22
2.2.4 Solution Procedure	22
2.3 Results and Discussion	22
2.3.1 Comparison With Finite Element Model	22
2.3.2 Failure Load Prediction	24
3. CONCLUSION	37
4. REFERENCES	38
APPENDIX A—BOUNDARY CONDITIONS FOR CLOSED FORM MODEL	

LIST OF FIGURES

Figure		Page
1	Specimen Geometry of ASTM D 1002	2
2	Specimen Geometry of ASTM D 3165	2
3	Specimen Geometry of ASTM D 5656	2
4	Deformed Shape After Load is Applied	3
5	Mounting of KGR-1 Device (ASTM D 5656)	4
6	Locations of A, B, C, D, E, and F	4
7	Rotation of Specimen and Coordinate Systems	4
8	Partial Finite Element Mesh Including the Adhesive Being Tested ($t = 1.016$ mm or 0.04 in.)	6
9	Adhesive Shear Stress Distribution ($t = 0.0254$ mm or 0.001 in.)	7
10	Adhesive Shear Stress Distribution ($t = 1.016$ mm or 0.04 in.)	8
11	Adhesive Shear Stress Distribution ($t = 2.032$ mm or 0.08 in.)	8
12	Calculated G_{ASTM} From Finite Element Model	10
13	F_a as a Function of t and G_{true}	12
14	F_b as a Function of t and G_{true}	13
15	F_c as a Function of t	14
16	Specimen Dimensions and Coordinate Systems	17
17	Free-Body Diagram and Sign Convention	20
18	Adhesive Shear Stress Distribution	24
19	Adhesive Peel Stress Distribution	24
20	Strength Prediction of Joints With Glass/Epoxy Adherends Based on First Data Group at $x_2 = 0$	28
21	Strength Prediction of Joints With Glass/Epoxy Adherends Based on Second Data Group at $x_2 = 0$	28

22	Strength Prediction of Joints With Glass/Epoxy Adherends Based on Third Data Group at $x_2 = 0$	29
23	Strength Prediction of Joints With Glass/Epoxy Adherends Based on Fourth Data Group at $x_2 = 0$	29
24	Strength Prediction of Joints With Glass/Epoxy Adherends Based on First Data Group at $x_2 = 0.02L_2$	30
25	Strength Prediction of Joints With Glass/Epoxy Adherends Based on Second Data Group at $x_2 = 0.02L_2$	30
26	Strength Prediction of Joints With Glass/Epoxy Adherends Based on Third Data Group at $x_2 = 0.02L_2$	31
27	Strength Prediction of Joints With Glass/Epoxy Adherends Based on Fourth Data Group at $x_2 = 0.02L_2$	31
28	Strength Prediction of Joints With Graphite/Epoxy Adherends Based on First Data Group at $x_2 = 0.02L_2$	32
29	Strength Prediction of Joints With Graphite/Epoxy Adherends Based on Second Data Group at $x_2 = 0.02L_2$	32
30	Strength Prediction of Joints With Graphite/Epoxy Adherends Based on Third Data Group at $x_2 = 0.02L_2$	33
31	Strength Prediction of Joints With Graphite/Epoxy Adherends Based on Fourth Data Group at $x_2 = 0.02L_2$	33
32	Strength Prediction of Joints With Glass/Epoxy Adherends Based on Strength Values From Coupon Tests	34
33	Strength Prediction of Joints With Graphite/Epoxy Adherends Based on Strength Values From Coupon Tests	34

LIST OF TABLES

Table		Page
1	Aspect Ratios of Finite Element Mesh	7
2	Recovered Adhesive Shear Modulus Based on Equation 9	11
3	Percentage of Each Term in Tsai-Hill Criterion and Strength Parameters Based on First Data Group with Glass/Epoxy Adherends	35
4	Percentage of Each Term in Tsai-Hill Criterion and Strength Parameters Based on Second Data Group With Glass/Epoxy Adherends	35
5	Percentage of Each Term in Tsai-Hill Criterion and Strength Parameters Based on Third Data Group With Glass/Epoxy Adherends	35
6	Percentage of Each Term in Tsai-Hill Criterion and Strength Parameters Based on Fourth Data Group With Glass/Epoxy Adherends	36
7	Percentage of Each Term in Tsai-Hill Criterion and Strength Parameters Based on First Data Group With Graphite/Epoxy Adherends	36
8	Percentage of Each Term in Tsai-Hill Criterion and Strength Parameters Based on Second Data Group With Graphite/Epoxy Adherends	36
9	Percentage of Each Term in Tsai-Hill Criterion and Strength Parameters Based on Third Data Group With Graphite/Epoxy Adherends	37
10	Percentage of Each Term in Tsai-Hill Criterion and Strength Parameters Based on Fourth Data Group With Graphite/Epoxy Adherends	37

EXECUTIVE SUMMARY

While the general aviation industry increasingly uses adhesive bonding for airframe composite structures, several issues have become important, namely, the qualification methods for adhesives used and the certification of adhesive joints. There is a lack of a generally agreed upon design methodology for adhesive-bonded composite joints, especially as it concerns the failure criterion.

There are two parts included in this report. The first part evaluates the most commonly used test method for adhesive properties, ADTM D 5656 "Standard Test Method for Thick-Adherend Metal Lap-Shear Joints for Determination of the Stress-Strain Behavior of Adhesives in Shear by Tension Loading." Finite element analyses were conducted to simulate the specimen behavior following the ASTM procedures. It was found that deviations of the measured adhesive shear modulus from the true value can be as large as 20% if corrections are not made. Correction factors based on different bondline thicknesses and adhesive properties are provided in the report.

There are generally three failure modes of adhesive-bonded composite joints: (1) adherend failure, (2) adhesive failure of the adhesive, and (3) cohesive failure of the adhesive. The second part of this report provides (1) an analytical model for predicting stress distributions within an adhesive-bonded composite joint using ASTM D 3165 test specimen dimensions and (2) a method for predicting joint strength under the adherend failure mode. The analytical model was verified using a finite element model and comparing the adhesive stress distributions of the two analyses. A failure analysis was conducted based on four failure criteria. Predicted strengths were compared with test data. It was shown that the maximum interlaminar axial tensile stress criteria predict the joint strength better than Tsai-Hill and von Mises criteria.

1. EVALUATION AND ADJUSTMENT OF ASTM D 5656 "STANDARD TEST METHOD FOR THICK-ADHEREND METAL LAP-SHEAR JOINTS FOR DETERMINATION OF THE STRESS-STRAIN BEHAVIOR OF ADHESIVES IN SHEAR BY TENSION LOADING."

1.1 INTRODUCTION.

With the introduction of high performance fibers such as carbon, boron, and Kevlar®, together with new and improved matrix materials, such as high-temperature thermoplastics, advanced composites have established themselves as engineering structural materials. An ideal structure should be designed without joints because joints are normally the weakest part of the structure. However, the need for assembly, disassembly, inspection, and repair means that some load-carrying joints cannot be avoided. Adhesive-bonded joints have been widely used for composite materials as a necessary alternative to conventional mechanical joint designs. The drawbacks of mechanical joining methods include (1) stress concentrations caused by drilled holes in laminates, (2) machining difficulties and subsequent damage to the composite laminates, and (3) weight penalty and fatigue associated with mechanical fasteners.

Reliable design of adhesive-bonded joints in which shear is a primary mode of load transfer requires knowledge of the material properties, including accurate adhesive strength and stiffness and failure criterion. However, as stated by Kutscha [1] and Kutscha and Hofer [2], among others, one of the greatest drawbacks to predicting the behavior of bonded joints has been the lack of reliable data on the mechanical properties of adhesives. If corrections are not made for Poisson's ratio constraints, the behavior of the adhesive in thin-film form appears to be different from the behavior of the adhesive in bulk form. Because of this, it is often suggested that specimens for determining mechanical properties should be of thin-film configurations. There still remains the difficulty of obtaining the pure shear or pure tensile stresses needed to determine the corresponding properties. Several commonly used ASTM standard tests on adhesives are listed as follows:

1. ASTM E 229 "Standard Method of Test for Shear Strength and Shear Modulus of Structural Adhesive."
2. ASTM D1002 "Standard Method of Test for Strength Properties of Adhesives in Shear by Tension Loadings (Metal-to-Metal)."
3. ASTM D 3165 "Strength Properties of Adhesives in Shear by Tension Loading of Single-Lap-Joint Laminated Assemblies."
4. ASTM D 5656 "Thick-Adherend Metal Lap-Shear Joints for Determination of Stress-Strain Behavior of Adhesives in Shear by Tension Loading."

Basically, ASTM E 229 is the so-called "Napkin Ring Test" where specimens are loaded in torsion, ASTM D 1002, 3165, and 5656 are single-lap shear tests where specimens are loaded in tension. Due to the lack of access to torsional testers, ASTM E 229 is not as popular as the other standard test methods.

Figures 1, 2, and 3 show the lap-shear specimens specified in ASTM D 1002, 3165, and 5656, respectively. Due to the eccentricity of the specimen geometry, the adherends rotate as a result of bending moment as shown in figure 4. This rotation introduces adhesive peel stress in the vicinity of the joint edges. Among the tests listed above, the ASTM D 5656 specimen has the advantages of the largest adherend cross-sectional area and largest bending rigidity, so it has the least adherend rotation and the lowest adhesive peel stress. On the other hand, ASTM D 1002 and D 3165 provide relative joint strength when results are compared among different adhesives but cannot readily determine adhesive modulus values or yield strength. Stress-strain curves can be obtained by ASTM D 5656 with an appropriate measuring device such as KGR-1 [3-7]. From the stress-strain curves, the mechanical characteristics of the adhesive can be determined.

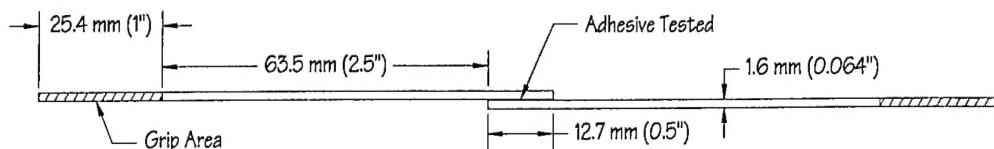


FIGURE 1. SPECIMEN GEOMETRY OF ASTM D 1002

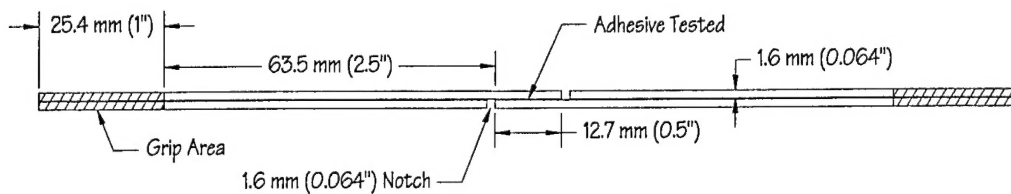


FIGURE 2. SPECIMEN GEOMETRY OF ASTM D 3165

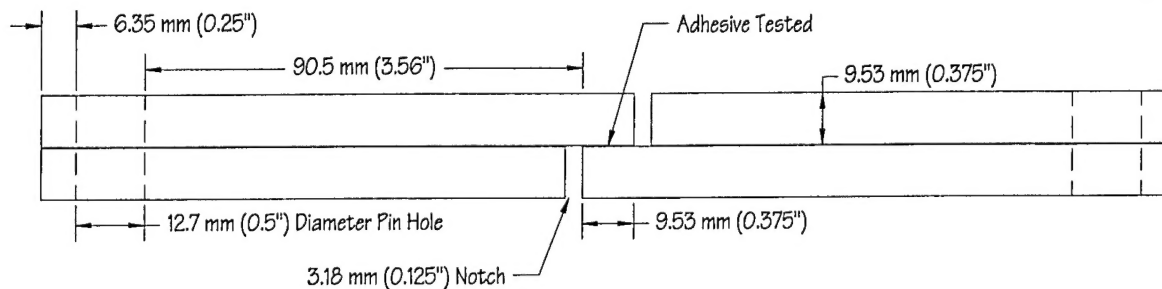


FIGURE 3. SPECIMEN GEOMETRY OF ASTM D 5656

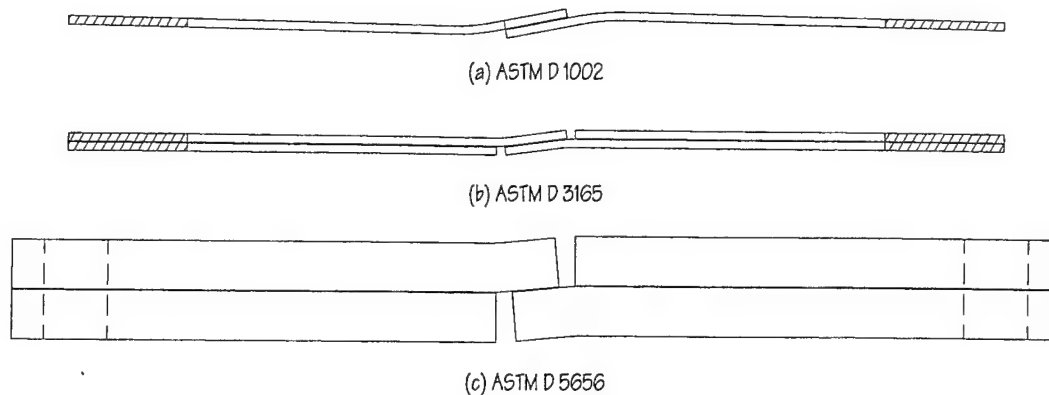


FIGURE 4. DEFORMED SHAPE AFTER LOAD IS APPLIED

Due to the shear-lag effect, the shear stress distribution within a lap joint is not uniform in the load direction. Furthermore, the shear stress nonuniformity in the through-thickness direction becomes appreciable if the bondline thickness exceeds certain values. Recently, Tsai, et al. [8] investigated the thick-adherend lap-shear test with three measuring techniques: KGR-1 extensometer, Moirè interferometry, and strain gage. In their study, nonuniformity of adhesive shear strain distribution and the corresponding correction factor were determined experimentally. The error in ASTM D 5656 that resulted from the slippage of measuring pins relative to the aluminum specimen was studied by Kassapoglou and Adelman [9].

In this present study, three sources of error in ASTM D 5656 were investigated: (1) the nonuniform shear stress-strain distribution within the test specimen, (2) the nonuniform shear strain distribution within the dummy all-aluminum specimen, and (3) the slippage of measuring pins with respect to the specimen. Through a finite element analysis, correction factors are provided to adjust the results from the current ASTM D 5656 so that the shear modulus of the tested adhesive can be recovered. Suggestions for mounting the KGR-1 device are also given to eliminate the error due to the slippage of the mounting pins.

1.2 ASTM D 5656 MEASUREMENT AND ANALYSIS.

Based on ASTM D 5656 procedure, the KGR-1 device (see figure 5) is mounted on the side of the test specimen with three mounting pins. These mounting pins are attached at locations A, B, and C on the side of the aluminum adherends as shown in figures 5 and 6. The KGR-1 device is designed to measure the relative displacement between B and C. The pin attached to A is used for alignment purposes because the joint region rotates after the load is applied. Therefore, the KGR-1 reading represents the relative displacement between B and C in the x direction, or specified as the "KGR" direction (parallel to the adherend-adhesive interface) as shown in figures 7.

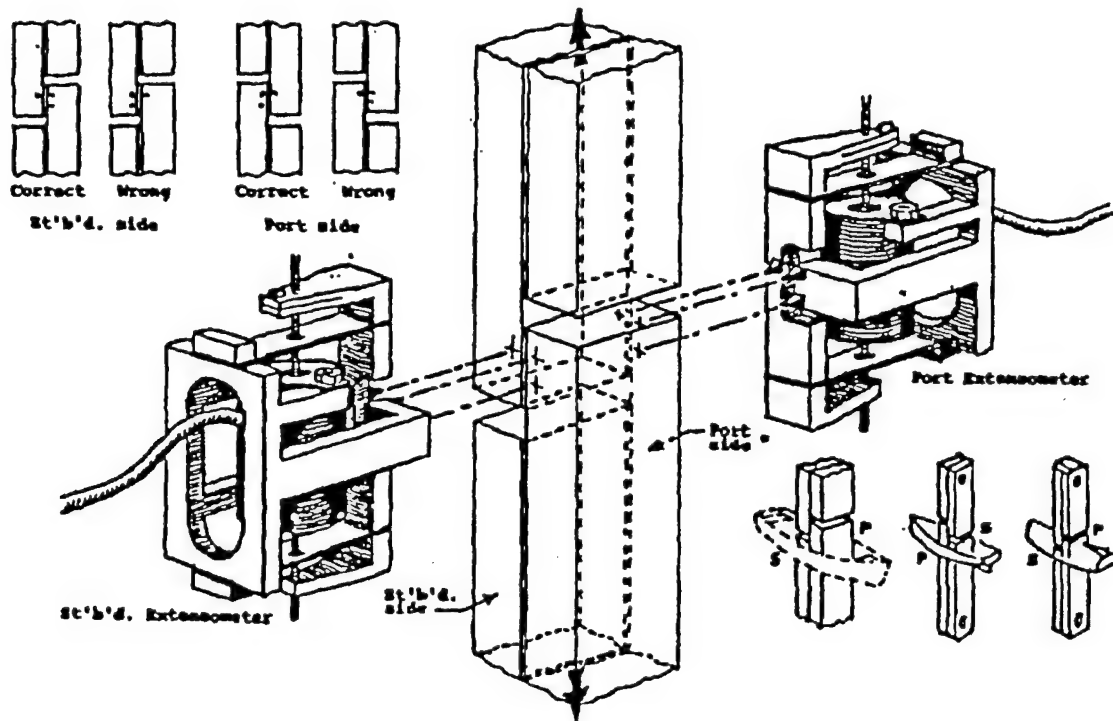


FIGURE 5. MOUNTING OF KGR-1 DEVICE (ASTM D 5656)

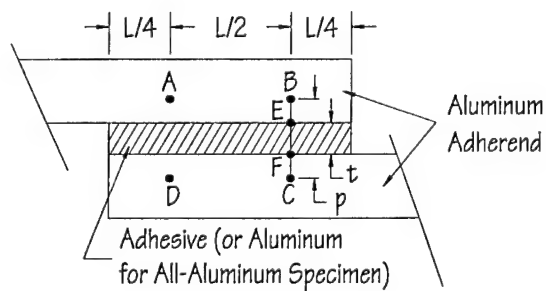


FIGURE 6. LOCATIONS OF A, B, C, D, E, AND F

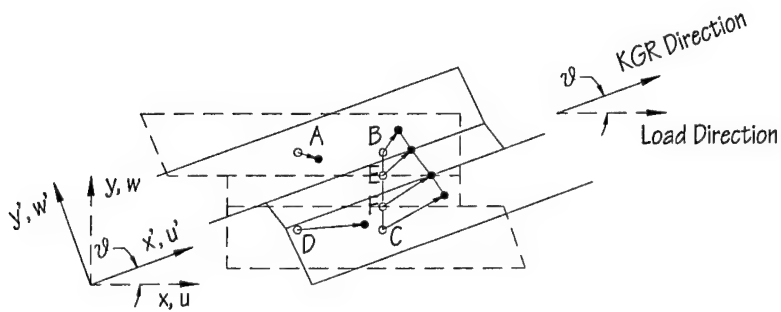


FIGURE 7. ROTATION OF SPECIMEN AND COORDINATE SYSTEMS

The apparent adhesive shear strain $\gamma_{apparent}$, which is used to calculate the adhesive shear modulus, is determined by

$$\gamma_{apparent} = \frac{d_a - d_m}{t} \quad (1)$$

where t is the adhesive thickness, d_a is the KGR-1 measurement representing the relative displacement between B and C in the KGR direction of the test specimen, and d_m is the portion of d_a caused by the displacements in the aluminum adherends. While d_a is obtained from the KGR-1 measurement on the normal specimen with a bond present, d_m is determined by testing an all-aluminum dummy specimen with the same dimensions as the specimen with the bond present but with the adhesive replaced by aluminum. The length d_m is calculated from

$$d_m = \frac{p - t}{p} M \quad (2)$$

where M is the KGR-1 measurement representing the relative displacement between B and C in the KGR direction of the all-aluminum dummy specimen, p is the distance between B and C, and t is the "aluminum bondline" thickness which is equivalent to the distance between E and F in figure 6.

The average adhesive shear stress average is calculated by

$$\tau_{average} = \frac{P}{Lb} \quad (3)$$

where P is the applied tensile load, L is the overlap length, and b is the width of the joint. After the apparent stress and strain are obtained, the linear shear modulus G_{ASTM} is then calculated as

$$G_{ASTM} = \frac{\tau_{average}}{\gamma_{apparent}} \quad (4)$$

1.3 SOURCES OF ERROR.

Basically, there are three sources of error based on the procedure and configurations specified in ASTM D 5656:

1. Due to the nonuniformity of the adhesive stress and strain distributions in the through-thickness and load directions, the $\gamma_{apparent}$ in equation 1 implies a certain degree of deviation from the actual average. As a result, the shear modulus obtained in equation 4 can deviate more than 15% from the true value depending on the material properties of the adhesive and the bondline thickness.
2. Equation 2 is based on the assumption of a linear displacement field in the all-aluminum sample from B to C. However, this is not true because of the different end conditions of

the material layers from B to E and from E to F. Therefore, the use of equation 2 to determine the portion of displacement from B to E and from F to C is not accurate.

3. Slippage occurs between the mounting pins of the KGR-1 device and the adherends at A and B. This is due to the stretching in the adherends between A and B under the tensile load and the fact that usually friction between the pins and the aluminum surface is the only mechanism which stops the slippage. Furthermore, once slippage occurs, either one or both of pins lose contact with A or B and the KGR-1 device reading is no longer correct. No corrections can be made since this slippage is totally out of control.

1.4 FINITE ELEMENT ANALYSIS.

Linear finite element analyses were conducted using ABAQUS [10 and 11] to model the mechanical behavior of the ASTM D 5656 normally bonded and all-aluminum dummy test specimens under loading. Eight-noded, two-dimensional plane-strain elements were used in this investigation. The shear moduli used in the finite element analysis ranged from 0.69 GPa (100 ksi) to 1.724 GPa (250 ksi) with a fixed Poisson's ratio of 0.33, these values cover the commonly used adhesives. The geometry of the ASTM D 5656 standard specimen, as shown in figure 3, was modeled with various adhesive bondline thicknesses from 0.0254 mm (0.001 in) to 3.048 mm (0.12 in). Figure 8 shows a close-up view of a portion of the finite element mesh with a bondline thickness of 1.016 mm (0.04 in). The number of elements in the finite element mesh through the adhesive thickness and the largest element aspect ratio for each of the adhesive thicknesses analyzed are listed in table 1. Under the applied tensile load of 4,448 N (1,000 lb), the shear stress distribution within the adhesive and the displacements of A, B, C, D, E, and F in both x and y direction were recorded. All-aluminum dummy specimens with various aluminum bondline thicknesses were also analyzed and the displacements of A, B, C, and D were recorded.

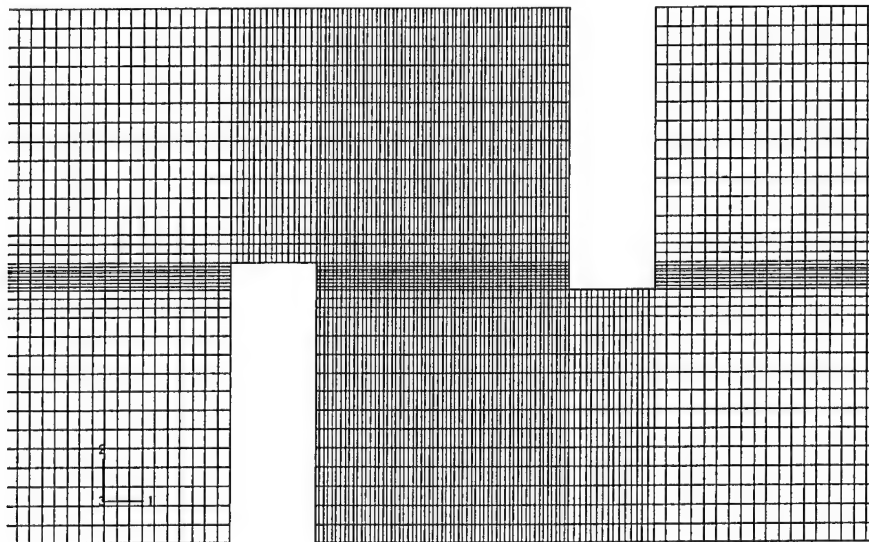


FIGURE 8. PARTIAL FINITE ELEMENT MESH INCLUDING THE ADHESIVE BEING TESTED ($t = 1.016$ mm or 0.04 in.)

TABLE 1. ASPECT RATIOS OF FINITE ELEMENT MESH

Adhesive Thickness, t	Number of Elements through Adhesive Thickness	Largest Element Aspect Ratio
0.0254 mm (0.001 in)	2	12.5
0.254 mm (0.01 in)	6	3.75
1.016 mm (0.04 in)	8	1.25
2.032 mm (0.08 in)	8	1.60
3.048 mm (0.12 in)	10	1.92

1.5 RESULTS AND DISCUSSION.

The shear stress distributions within the test region are shown in figures 9, 10, and 11 for different bondline thicknesses under a tensile load of 4,448 N (1,000 lb). The three curves specified as top, middle, and bottom represent the shear stress of the adhesive at the upper adhesive-adherend interface, center of the adhesive layer, and the lower adhesive-adherend interface, respectively. As expected, the peak adhesive shear stresses and strains are located at the edges of the overlap and the adhesive shear stress and strain are not uniform through the bondline thickness. It can also be seen that the thinner the bondline thickness, the higher the peak adhesive shear stress and strain occur at the edges of the overlap. Because the total shear force is equal to the total applied tensile force, the higher the peak adhesive shear stress at the edges of the overlap, the lower the shear stress present in the central region of the overlap. Because ASTM D 5656 uses the average through-thickness adhesive shear strain between E and F as the apparent shear strain to calculate the shear modulus, the lower the shear strain at the central region of the overlap, the higher the shear modulus obtained from the test.

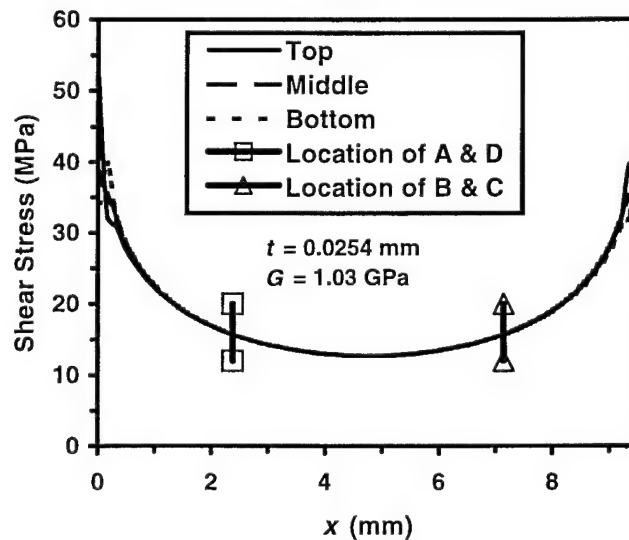


FIGURE 9. ADHESIVE SHEAR STRESS DISTRIBUTION
($t = 0.0254$ mm or 0.001 in.)

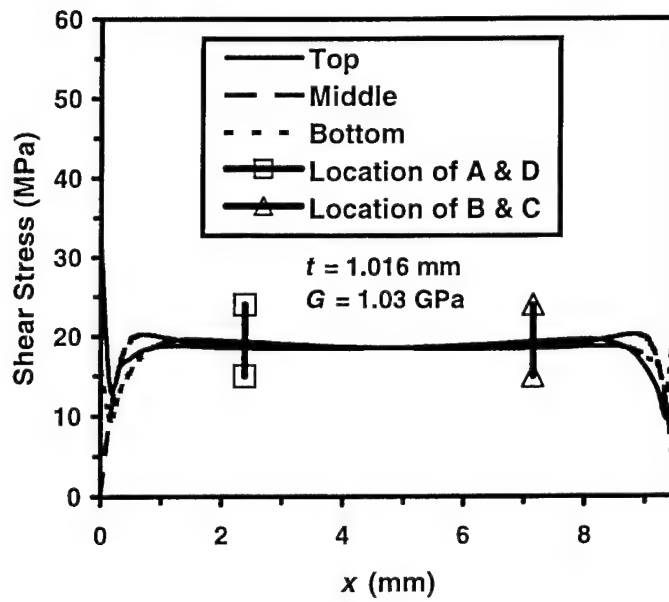


FIGURE 10. ADHESIVE SHEAR STRESS DISTRIBUTION
($t = 1.016$ mm or 0.04 in.)

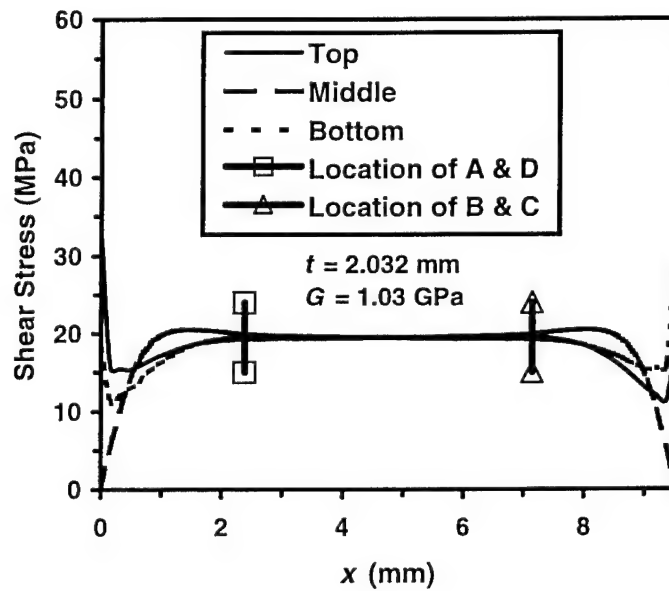


FIGURE 11. ADHESIVE SHEAR STRESS DISTRIBUTION
($t = 2.032$ mm or 0.08 in.)

The following derivations describe how the finite element results were used to simulate the ASTM D 5656 procedure and the associated results. The relative displacement of E and F in the KGR direction $u'_E - u'_F$ (figure 7) can be calculated as

$$u'_F - u'_E = u_F - u_E - \theta t \quad (5)$$

where u'_F and u'_E are the displacements of F and E in the KGR direction, u_F and u_E are the displacements of F and E in the x direction, respectively, t is the bondline thickness and θ is the angle of rotation of the overlap (figure 7) which can be determined by

$$\theta = \frac{(w_B - w_A)}{L/2} \quad (6)$$

where w_A and w_B are the displacements of A and B in the y direction (figure 7), respectively, and L is the length of the overlap (9.53 mm, 0.375"). It should be noted that the u_F , u_E , w_A , and w_B on the right-hand side of equations 5 and 6 are obtained directly from finite element analysis. The θ in equation 6 is the rotation of the upper adherend because it is calculated based on the displacements of A and B. It was confirmed that the rotation of the lower adherend, based on w_C and w_D , is almost the same as the rotation of the upper adherend with a difference less than 0.001%.

Once the relative displacement of E and F in the KGR direction is determined, the average adhesive shear strain between E and F is then

$$\gamma_{EF} = \frac{u'_F - u'_E}{t} \quad (7)$$

Replacing the $\gamma_{apparent}$ in equation 1 with the γ_{EF} in equation 7 and substituting equation 1 and the $\gamma_{apparent}$ in equation 3 into equation 4, the adhesive shear modulus G_{ASTM} is then determined as

$$G_{ASTM} = \frac{F}{Lb \frac{u'_F - u'_E}{t}} \quad (8)$$

where b (25.4 mm, 1") is the width of the overlap and F is the applied tensile load.

Figure 12 shows the calculated G_{ASTM} as a function of bondline thickness based on equation 8 with u'_F and u'_E determined from finite element analysis. The horizontal lines represent the "true" shear moduli G_{true} of the adhesive, i.e., the values used in the finite element computations. It can be seen that, due to the different degrees of nonuniformity of the shear strain along the overlap length, the calculated adhesive shear modulus varies with both the adhesive bondline thickness and the shear modulus. The calculated G_{ASTM} can deviate as much as 20% from G_{true} . It is also interesting to observe that, among adhesives with different stiffnesses, when the bondline thickness is about 0.51 mm (0.02"), the calculated G_{ASTM} is very close to G_{true} .

Therefore, it is suggested that a bondline thickness of approximately 0.51 mm (0.02") is an optimal thickness when testing adhesive shear modulus using ASTM D 5656. A nonlinear regression was conducted among these data points as a method of recovering G_{true} from G_{ASTM} . A linear function between $G_{recovered}$ and G_{ASTM} was obtained in the form of

$$G_{recovered} = C_1 G_{ASTM} + C_2 \quad (9)$$

$$\begin{cases} C_1 = 1.03t^{0.068} \\ C_2 = -0.000483 + 0.073e^{-3.29t} \end{cases} \text{ for } t \text{ in mm and } G \text{ in GPa} \quad (10)$$

and

$$\begin{cases} C_1 = 1.28t^{0.068} \\ C_2 = -0.07 + 10.58e^{-83.62t} \end{cases} \text{ for } t \text{ in inch and } G \text{ in ksi} \quad (11)$$

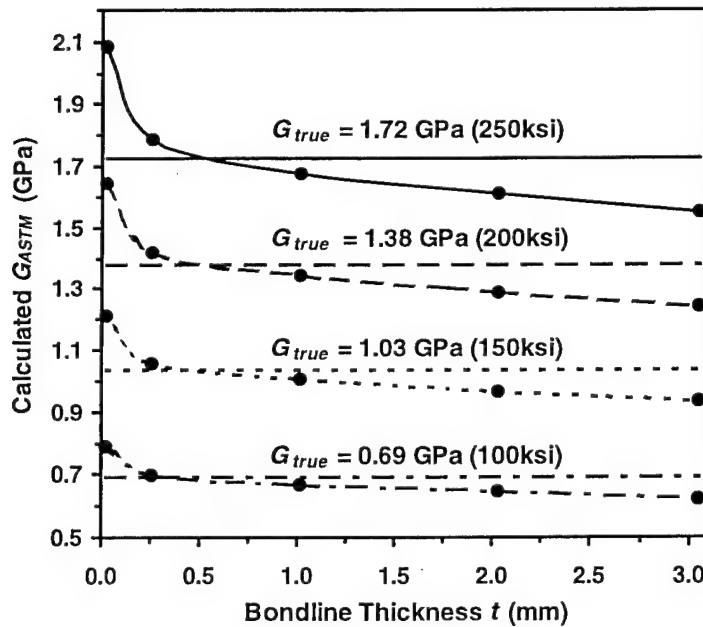


FIGURE 12. CALCULATED G_{ASTM} FROM FINITE ELEMENT MODEL

Table 2 is a list of G_{ASTM} , G_{true} , and the $G_{recovered}$ determined by equations 10 and 11 for both SI and English units, respectively. It can be seen that, after the correction is made, the shear moduli recovered from the ASTM test deviate from the true values by less than 1.5%.

TABLE 2. RECOVERED ADHESIVE SHEAR MODULUS BASED ON EQUATION 9

	G_{ASTM}	G_{true}	$G_{recovered}$
$t = 0.0254 \text{ mm (0.001 in)}$	2.083 GPa (302 ksi)	1.724 GPa (250 ksi)	1.737 GPa (251 ksi)
$C_1 = 0.802 (0.800)$	1.645 GPa (239 ksi)	1.379 GPa (200 ksi)	1.386 GPa (201 ksi)
$C_2 = 0.0667 (9.66)$	1.211 GPa (176 ksi)	1.034 GPa (150 ksi)	1.038 GPa (150 ksi)
	0.785 GPa (114 ksi)	0.690 GPa (100 ksi)	0.696 GPa (101 ksi)
$t = 0.254 \text{ mm (0.01 in)}$	1.785 GPa (259 ksi)	1.724 GPa (250 ksi)	1.706 GPa (247 ksi)
$C_1 = 0.938 (0.936)$	1.417 GPa (205 ksi)	1.379 GPa (200 ksi)	1.360 GPa (196 ksi)
$C_2 = 0.0312 (4.51)$	1.054 GPa (153 ksi)	1.034 GPa (150 ksi)	1.020 GPa (148 ksi)
	0.696 GPa (101 ksi)	0.690 GPa (100 ksi)	0.684 GPa (99 ksi)
$t = 1.016 \text{ mm (0.04 in)}$	1.678 GPa (243 ksi)	1.724 GPa (250 ksi)	1.732 GPa (250 ksi)
$C_1 = 1.031 (1.028)$	1.340 GPa (194 ksi)	1.379 GPa (200 ksi)	1.384 GPa (200 ksi)
$C_2 = .00210 (0.303)$	1.004 GPa (146 ksi)	1.034 GPa (150 ksi)	1.037 GPa (150 ksi)
	0.669 GPa (97 ksi)	0.690 GPa (100 ksi)	0.692 GPa (100 ksi)
$t = 2.032 \text{ mm (0.08 in)}$	1.610 GPa (234 ksi)	1.724 GPa (250 ksi)	1.740 GPa (252 ksi)
$C_1 = 1.081 (1.078)$	1.288 GPa (187 ksi)	1.379 GPa (200 ksi)	1.392 GPa (202 ksi)
$C_2 = -0.00039 (-0.0568)$	0.966 GPa (140 ksi)	1.034 GPa (150 ksi)	1.044 GPa (151 ksi)
	0.644 GPa (93.5 ksi)	0.690 GPa (100 ksi)	0.696 GPa (101 ksi)
$t = 3.048 \text{ mm (0.12 in)}$	1.551 GPa (225 ksi)	1.724 GPa (250 ksi)	1.723 GPa (249 ksi)
$C_1 = 1.111 (1.108)$	1.241 GPa (180 ksi)	1.379 GPa (200 ksi)	1.378 GPa (199 ksi)
$C_2 = -0.00048 (-0.0695)$	0.932 GPa (135 ksi)	1.034 GPa (150 ksi)	1.035 GPa (150 ksi)
	0.621 GPa (90.1 ksi)	0.690 GPa (100 ksi)	0.689 GPa (99.8 ksi)

One other error comes from the values of $u'_F - u'_E$ which are used in equation 8 to determine G_{ASTM} . Based on the ASTM procedure described earlier (see equations 1 and 2), $u'_F - u'_E$ is equal to $d_a - d_m$;

$$d_a = u'_C - u'_B \quad (12)$$

where d_a is the direct reading from KGR-1 device when testing ASTM D 5656 specimen, and

$$d_m = \frac{p-t}{p} M = \frac{p-t}{p} (u'_{C,M} - u'_{B,M}) \quad (13)$$

The subscript “M” denotes the all-aluminum dummy specimen and d_m is assumed to be $(u'_C - u'_F) + (u'_E - u'_B)$. However, d_m is equal to $(u'_C - u'_F) + (u'_E - u'_B)$ only under the condition that the shear strain distribution within an aluminum-adhesive specimen and an all-aluminum specimen are the same and that the shear strain between B and C of the all-aluminum specimen in the x direction is constant. Due to the nonconstant shear strain between B and C in the all-aluminum specimen, a correction factor F_a is needed to convert d_m into $(u'_C - u'_F) + (u'_E - u'_B)$

$$(u'_C - u'_F) + (u'_E - u'_B) = F_a d_m \quad (14)$$

Figure 13 shows F_a as a function of adhesive shear modulus G_{true} and bondline thickness. It can be seen that the change of F_a for varying adhesive shear modulus is almost negligible. A linear regression yields F_a as a function of bondline thickness as

$$F_a = -0.0683t + 1.065 \quad \text{for } t \text{ in mm} \quad (15)$$

$$F_a = -1.73t + 1.065 \quad \text{for } t \text{ in inch} \quad (16)$$

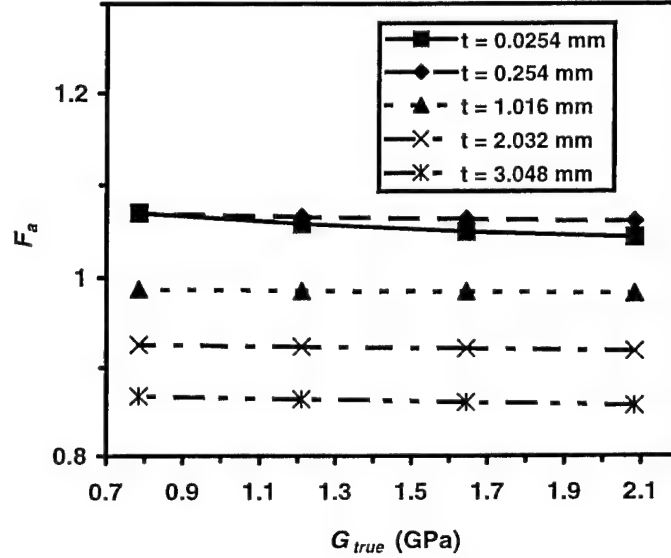


FIGURE 13. F_a AS A FUNCTION OF t AND G_{true}

The scatter in the results of most ASTM D 5656 tests come from the slippage of the mounting pins of the KGR-1 device. Slippage occurs because of the stretching of the adherend between A and B under tensile loading. Even though the stretching of the adherend is very small, considerable error will occur because the displacement, due to shear strain of the adhesive, is also very small. The unpredictable nature of the mounting pin slippage further increases the difficulty in correcting it. If holes corresponding to the size of the pins are drilled at A, B, and C in the adherends and the KGR-1 device is mounted to the specimen by inserting the mounting pins into the holes, the scatter is eliminated and the error due to stretching can then be predicted and corrected. Based on the assumption that one of the two arms of KGR-1 device which is attached to the adherend through two pins at A and B moves according to the average displacement of A and B, the measurement taken by KGR-1 device is then the relative displacement between C and the midpoint of A and B. In other words, the KGR-1 readings represent $u'_C - (u'_A + u'_B) / 2$. In order to adjust the KGR-1 reading so that it represents $u'_C - u'_B$, another correction factor F_b is needed so that

$$u'_C - u'_B = F_b \left[u'_C - \frac{(u'_A + u'_B)}{2} \right] \quad (17)$$

Figure 14 shows F_b as a function of t and G_{true} based on the results from finite element analysis. Nonlinear regression gives the following equations:

$$F_b = C_3 G_{true} + C_4 \quad (18)$$

where

$$\begin{cases} C_3 = 0.0157t - 0.0588 \\ C_2 = 1 - 0.398e^{-7.89t} \end{cases} \text{ for } t \text{ in mm and } G \text{ in GPa} \quad (19)$$

$$\begin{cases} C_3 = 0.00275t - 0.000405 \\ C_2 = 1 - 0.398e^{-200t} \end{cases} \text{ for } t \text{ in inch and } G \text{ in ksi} \quad (20)$$

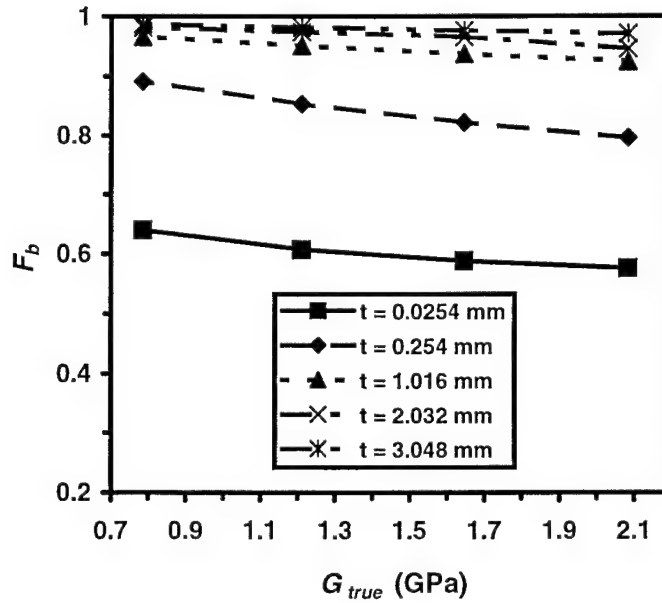


FIGURE 14. F_b AS A FUNCTION OF t AND G_{true}

The same argument can be applied to the readings of the all-aluminum specimen. Again, if holes are drilled and the KGR-1 device is attached to the all-aluminum specimen by inserting the mounting pins into the holes, the resultant scatter is again eliminated. A correction factor F_c is then needed to adjust the KGR reading to the real ($u'_{C,M} - u'_{B,M}$)

$$u'_{C,M} - u'_{B,M} = F_c \left[u'_{C,M} - \frac{(u'_{A,M} + u'_{B,M})}{2} \right] \quad (21)$$

Figure 15 shows F_c values for the five selected bondline thicknesses based on the finite element results and the curve-fit result as a second-order polynomial:

$$F_c = 0.0263t^2 + 0.175t + 0.521 \quad \text{for } t \text{ in mm} \quad (22)$$

$$F_c = 17t^2 + 4.45t + 0.521 \quad \text{for } t \text{ in inch} \quad (23)$$

The use of F_b and F_c can be eliminated if four pins and holes are used to mount the KGR-1 device. In other words, each arm of the KGR-1 device is attached to the adherend through two pins. One arm is attached to A and B and the other arm attached to C and D as shown in figure 6. With the assumption that each arm represents the average displacement between either A and B or C and D, it is shown by the finite element results that, due to the anti-symmetric geometry and loading of the joint system

$$u'_C - u'_B = \frac{(u'_C + u'_D)}{2} - \frac{(u'_A + u'_B)}{2} \quad (24)$$

Therefore, it is suggested that the four-pin arrangement with the four pins inserted into the adherends be used to attach the KGR-1 device. By doing so, there will be no need for the correction factors F_b and F_c .

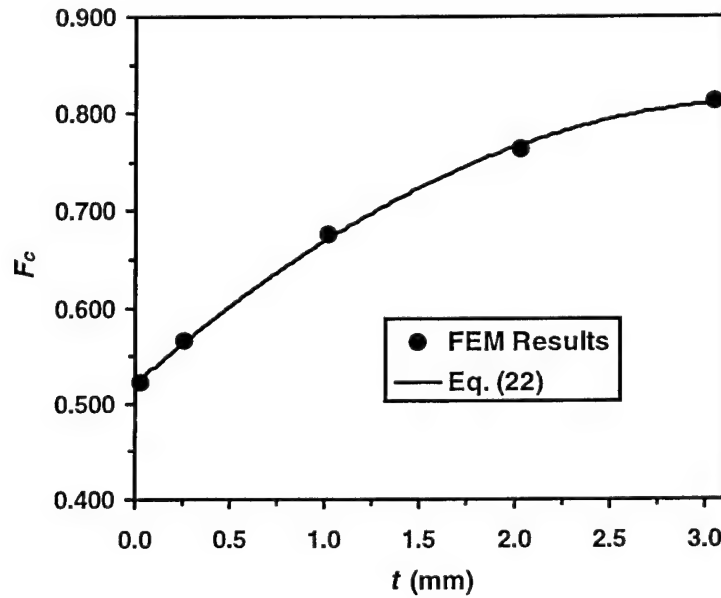


FIGURE 15. F_c AS A FUNCTION OF t

2. STRESS MODEL AND INTERLAMINAR FAILURE OF ADHESIVE-BONDED COMPOSITE JOINTS USING ASTM D 3165 SPECIMENS.

2.1 INTRODUCTION.

Advanced composite materials have been widely used due to their light weight and high corrosion resistance. In many of these applications, bolted joints have been replaced by adhesive-bonded joints because of the weight penalty and fatigue associated with mechanical fasteners. Many certification-related issues become more important as the application of adhesive-bonded joints gains its popularity in the general aviation industry. One of these concerns has been the use of thick bondlines. The purpose of this investigation is to develop an analytical model to determine the stress distributions within an adhesive-bonded single-lap composite joint and to use the model to analyze and predict the joint strength.

The earlier studies on adhesive-bonded joints can be found from the review papers by Kutscha [1], Kutscha and Hofer [2], Matthews, et al. [12], and Vinson [13]. When studying adhesive-bonded lap joints, the effects due to the rotation of the adherends were first taken into account by Goland and Reissner [14]. They introduced an equation to relate the bending moment of the adherend at the end of the overlap to the in-plane loading. The basic approach of the Goland and Reissner theory was based on beam theory, or rather, on cylindrically bent-plate theory which treated the overlap section as a beam of twice the thickness of the adherend. Hart-Smith [15-18] published a series of papers regarding single-lap, double-lap, scarf, and stepped-lap joints involving a continuum mechanics model in which the adherends were isotropic or anisotropic elastic, and the adhesive was modeled as elastic, elastic-plastic, or bielastic. Basically, classical plate theory was adopted during Hart-Smith's derivation. However, the effects of transverse shear deformation, which has been shown to be important when the span-to-depth ratio is small or when the transverse shear modulus is small (Reissner [19] and Reddy [20]), were not included in either Goland and Reissner or Hart-Smith's theories. Moreover, edge effects were neglected and adhesive stresses were assumed constant through the thickness in most of the analyses found in the literature.

Renton and Vinson [21] utilized a higher order formulation to analyze adhesive-bonded joints that included the adherend transverse shear and normal strains. Their results were compared with photoelastic experiments and show excellent agreement except for local stress concentrations at the edges of the overlap region. Griffin, et al. [22] researched adhesive-bonded composite pipe joints and developed a mathematical model on the stress-strain behavior of such joints. Yang, et al. [23] studied double-lap composite joints under cantilevered bending and developed a strain gap model to describe the stress-strain behavior. Yang and Pang [24 and 25] also developed analytical models for adhesive-bonded composite single-lap joints under cylindrical bending and tension based on the laminated anisotropic plate theory. Their approach correlated the asymmetry of the adherend laminates as well as the effects due to the transverse shear deformation. More recently, Oplinger [26] studied single-lap joints with isotropic adherends and found that many of the predictions of the Goland-Reissner analysis are recovered in the limit of large adherend-to-adhesive layer thickness ratios, although substantial differences from the Goland-Reissner analysis can occur for relatively thin adherends.

Strength of adhesive-bonded double-lap composite joints were studied by Tong [27] in 1997. Due to the fact that the failure often occurs at the resin-fiber interface adjacent to the adhesive, Tong used a simplified one-dimensional model as well as finite element model in conjunction with several existing and new interlaminar failure criteria to predict the strength of the joints. In 1996, Adams and Davies [28] published the results based on their nonlinear finite element analysis on single-lap adhesive-bonded joints of composite/steel and composite/aluminum with different taper arrangement at the edges of the joints. Experimental study of the effects of adherend lay-up sequence on the joint strength following ASTM D 1002 was published by Thomas, et al. [29] in 1998.

Fracture mechanics approach was pursued by Chiang together with Chai [30 and 31]. They published a series of papers regarding the crack propagation criterion with both an end-notched flexure specimen and the butterfly specimens. Their results were verified by micrographic examination. Aluminum adherend was used in their investigation so only adhesive failure was studied. Ju, et al. [32] used the finite element method together with the continuum damage mechanics approach to evaluate the fatigue life of J-led solder joints. Dynamic crack growth of the bondline was investigated by Needleman and Rosakis [33]. Kinloch, et al. [34] used a local singular-field approach as well as a global method based on a consideration of the applied energy release rate to study the fixed-ratio mixed-mode delamination of fiber composites.

The finite element method has been widely used to analyze adhesive-bonded composite structures as well as adhesive-bonded repairs. Among these researchers, Charalambides, et al. [35 and 36] studied the bonded repairs under static and fatigue loading experimentally as well as using elastic-plastic finite element models, Kinloch, et al. [37], Jethwa and Kinloch [38] studied the fatigue behavior of adhesive joints.

In the present study, an analytical model was developed to determine the stress and strain distributions of adhesive-bonded composite single-lap joints under tension. The laminated anisotropic plate theory was applied in the derivation of the governing equations of the two bonded laminates. In order for the model to cover thick bondlines, theory of elasticity was applied to determine the mechanical behavior of the adhesive. With this approach, the adhesive stresses can vary through the bondline thickness. Both the adherend and the adhesive were assumed linear elastic in the derivations. The entire coupled system was then determined through the kinematics and force equilibrium of the adhesive and the adherends. The solutions to the overall system of governing equations were obtained by directly solving the differential equations with appropriate boundary conditions as well as the application of energy method (Ritz Method). Computer software Maple V was used as the calculation tool. Results from the analytical model were verified by finite element analysis using ABAQUS.

The three major failure modes of adhesive-bonded joints are (1) cohesive failure, (2) adhesive failure, and (3) adherend failure. While the first and second modes occur in most of the joints with metallic adherends, the third failure mode is the most common failure mode of bonded joints with composite laminates. Even though the developed model in the present investigation was based on linear elastic adhesive and adherend, it is appropriate to apply the developed model to analyze the adherend failure mode with first-ply failure criterion. ASTM D3165 specimen specification was used for both analytical model and experimental evaluations. Joint specimens

with Hysol EA 9394 structural paste adhesive and both carbon/epoxy and glass/epoxy adherends were tested for strength. All failed joints were examined for failure mode, and only the joints that failed under adherend failure mode were used for this present analysis. Four failure criteria, Tsai-Hill failure criterion, von Mises failure criterion, maximum interlaminar tensile stress criterion, and maximum tensile stress criterion were adopted to correlate the critical adherend stresses with failure load. Nonlinear regression was conducted in order to obtain the needed parameters in Tsai-Hill and von Mises failure criteria. These parameters include the tensile, interlaminar tensile, and shear strengths of the adherend for the Tsai-Hill criterion and the allowable von Mises stress for von Mises failure criterion. Experimental results from composite laminate coupon tests were used for maximum interlaminar tensile stress criterion, maximum tensile stress criterion, and Tsai-Hill criterion. It was found that the maximum interlaminar tensile stress criterion and the maximum tensile stress criterion provide better estimate of joint strength for the adherend failure mode. Under the assumption that the adhesive has the same characteristics when a bondline is formed with different thicknesses, the different joint strengths for various bondline thicknesses can be explained by the difference in stress distributions.

2.2 MODEL DERIVATION.

Figure 16 shows the configuration of a single-lap joint following ASTM D 3165 specification which was used in the current investigation. The tensile load, defined as P , represents the load per unit width. The joint was divided into three regions for convenience in the model development, where Region 2 is the overlap region being tested. The size of the notches was treated as zero in the model development. In other words, even though there is a discontinuity in the lower adherend between Region 1 and Region 2, the right end of Region 1, where $x_1 = L_1$, is located at the same position as the left end of Region 2 where $x_2 = 0$.

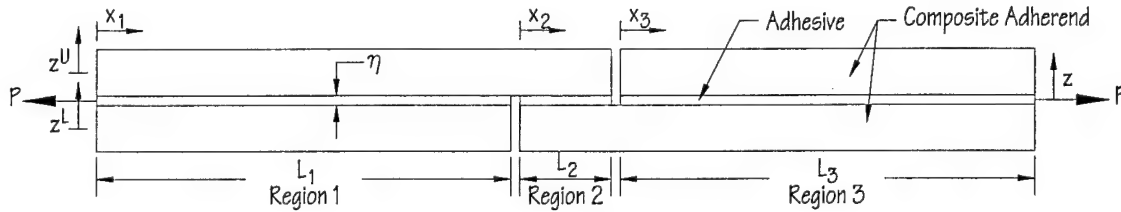


FIGURE 16. SPECIMEN DIMENSIONS AND COORDINATE SYSTEMS

2.2.1 Adherend Formulation.

The generalized formulas of the adherend and adhesive are the same for all three regions. The upper and lower adherends are assumed to follow the first-order laminated plate theory. The displacement field of the two adherends, u in the x direction and w in the z direction, can be written as

$$u^U = u^{oU}(x) + z^U \psi^U(x) \quad (25)$$

$$u^L = u^{oL}(x) + z^L \psi^L(x) \quad (26)$$

$$w^U = w^U(x) \quad (27)$$

$$w^L = w^L(x) \quad (28)$$

where superscript U and L denote the upper and lower adherend, respectively, superscript o represents the mid-plane displacement and ψ is the corresponding bending slope. Substitution of equations 25 through 28 into the strain-displacement relations yields the normal strain ε_x and shear strain γ_{xy} of the upper and lower adherends as

$$\varepsilon_x^U = \frac{du^U}{dx} = \frac{du^{oU}(x)}{dx} + z^U \frac{d\psi^U(x)}{dx} \quad (29)$$

$$\varepsilon_x^L = \frac{du^L}{dx} = \frac{du^{oL}(x)}{dx} + z^L \frac{d\psi^L(x)}{dx} \quad (30)$$

$$\gamma_{xz}^U = \frac{du^U}{dz^U} + \frac{dw^U}{dx} = \psi^U(x) + \frac{dw^U(x)}{dx} \quad (31)$$

$$\gamma_{xz}^L = \frac{du^L}{dz^L} + \frac{dw^L}{dx} = \psi^L(x) + \frac{dw^L(x)}{dx} \quad (32)$$

Together with the equivalent modulus matrices A , B , and D for orthotropic laminates, the normal stress resultant N_x , bending moment for unit width M_y , and transverse shear stress resultant Q_z , can be obtained as

$$N_x^U = A_{11}^U \frac{du^{oU}(x)}{dx} + B_{11}^U \frac{d\psi^U(x)}{dx} \quad (33)$$

$$N_x^L = A_{11}^L \frac{du^{oL}(x)}{dx} + B_{11}^L \frac{d\psi^L(x)}{dx} \quad (34)$$

$$M_y^U = B_{11}^U \frac{du^{oU}(x)}{dx} + D_{11}^U \frac{d\psi^U(x)}{dx} \quad (35)$$

$$M_y^L = B_{11}^L \frac{du^{oL}(x)}{dx} + D_{11}^L \frac{d\psi^L(x)}{dx} \quad (36)$$

$$Q_z^U = kA_{55}^U \left(\psi^U(x) + \frac{dw^U(x)}{dx} \right) \quad (37)$$

$$Q_z^L = kA_{55}^L \left(\psi^L(x) + \frac{dw^L(x)}{dx} \right) \quad (38)$$

where the equivalent stiffness A_{11} , B_{11} , D_{11} , and A_{55} for the upper and lower adherends are calculated based on

$$(A_{11}^U, B_{11}^U, D_{11}^U) = \int_{-h^U/2}^{h^U/2} Q_{11}^{(i)U} [I, z^U, (z^U)^2] dz^U \quad (39)$$

$$(A_{11}^L, B_{11}^L, D_{11}^L) = \int_{-h^L/2}^{h^L/2} Q_{11}^{(i)L} [I, z^L, (z^L)^2] dz^L \quad (40)$$

$$A_{55}^U = \int_{-h^U/2}^{h^U/2} Q_{55}^{(i)U} dz^U \quad (41)$$

$$A_{55}^L = \int_{-h^L/2}^{h^L/2} Q_{55}^{(i)L} dz^L \quad (42)$$

The $Q_{11}^{(i)}$ and $Q_{55}^{(i)}$ represent the tensile stiffness in x direction and the transverse shear stiffness of the i^{th} ply, respectively, h^U is the thickness of the upper adherend, h^L is the thickness of the lower adherend, and k is the shear correction factor.

In order to establish the equations of equilibrium, a free-body diagram of the laminates and adhesive is shown in figure 17. The equations for force equilibrium are then

$$\frac{dN_x^U}{dx} = -\tau^U \quad (43)$$

$$\frac{dN_x^L}{dx} = \tau^L \quad (44)$$

$$\frac{dM_y^U}{dx} = Q_z^U + \frac{h^U}{2} \tau^U \quad (45)$$

$$\frac{dM_y^L}{dx} = Q_z^L + \frac{h^L}{2} \tau^L \quad (46)$$

$$\frac{dQ_z^U}{dx} = q^U \quad (47)$$

$$\frac{dQ_z^L}{dx} = -q^L \quad (48)$$

where τ^U and q^U are the adhesive shear stress and peel stress (normal stress in z direction), respectively, at the upper adherend/adhesive interface, τ^L and q^L are the shear and peel stresses of the adhesive at the lower adherend/adhesive interface.

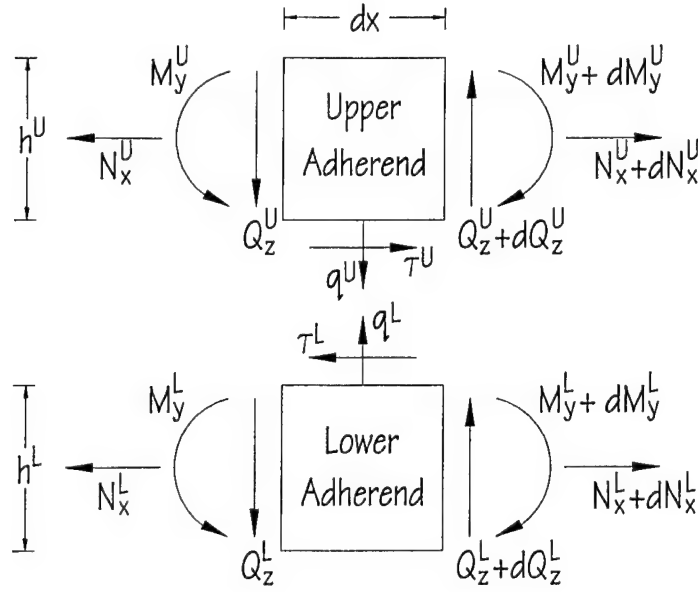


FIGURE 17. FREE-BODY DIAGRAM AND SIGN CONVENTION

2.2.2 Adhesive Formulation.

The adhesive displacement in x direction, u_a , and the displacement in z direction, w_a , are assumed to be polynomials of both x and z with undetermined coefficients A_m and B_m ($m = 1, 2, 3, \dots, n$) as

$$u_a = u_o(x, z) + \sum_m A_m u_m(x, z) = u_o(x, z) + (z + \frac{\eta}{2})(z - \frac{\eta}{2})(A_1 + A_2 x + A_3 z + \dots) \quad (49)$$

$$w_a = w_o(x, z) + \sum_m B_m w_m(x, z) = w_o(x, z) + (z + \frac{\eta}{2})(z - \frac{\eta}{2})(B_1 + B_2 x + B_3 z + \dots) \quad (50)$$

where u_o and w_o are linear functions of z which satisfy the continuity at the upper and lower interfaces between the adhesive and adherend where $z = \eta/2$ and $z = -\eta/2$. Therefore, u_o and w_o are related to the displacements of the adherends as

$$u_o(x, z) = \frac{1}{2} u^{oU}(x) - \frac{1}{4} h^U \psi^U(x) + \frac{1}{2} u^{oL}(x) + \frac{1}{4} h^L \psi^L(x) - \frac{z}{2\eta} [-2u^{oU}(x) + h^U \psi^U(x) + 2u^{oL}(x) + h^L \psi^L(x)] \quad (51)$$

$$w_o(x, z) = \frac{1}{2} w^U(x) + \frac{1}{2} w^L(x) + \frac{z}{\eta} [w^U(x) - w^L(x)] \quad (52)$$

Under plane-strain condition, the adhesive peel stress $\sigma_{a,z}$, and shear stress $\tau_{a,xz}$ can be determined in terms of the adhesive displacements as

$$\sigma_{a,z} = \frac{E}{1-\nu} \frac{\partial w_a}{\partial z} \quad (53)$$

$$\tau_{a,xz} = G \left(\frac{\partial u_a}{\partial z} + \frac{\partial w_a}{\partial x} \right) \quad (54)$$

where E and G are the Young's modulus and shear modulus of the adhesive, respectively, and ν is the Poisson's ratio of the adhesive.

The shear and peel stresses at the interfaces between the adhesive and adherends can be represented as the stresses at the upper and bottom surface of the adhesive.

$$\tau^U = -(\tau_{a,xz})_{@z=\eta/2} \quad (55)$$

$$\tau^L = -(\tau_{a,xz})_{@z=-\eta/2} \quad (56)$$

$$q^U = (\sigma_{a,z})_{@z=\eta/2} \quad (57)$$

$$q^L = (\sigma_{a,z})_{@z=-\eta/2} \quad (58)$$

The strain energy U in the adhesive can be written as:

$$\begin{aligned} U &= \frac{E}{2(1+\nu)} \iint \left[\frac{1}{1-\nu} \left(\frac{\partial w}{\partial z} \right)^2 + \frac{1}{2} \left(\frac{\partial w}{\partial x} + \frac{\partial u}{\partial z} \right)^2 \right] dx dz \\ &= \frac{E}{2(1+\nu)} \int_{-\eta/2}^{\eta/2} \left[\int_0^l \left[\frac{1}{1-\nu} \left(\frac{\partial w}{\partial z} \right)^2 + \frac{1}{2} \left(\frac{\partial w}{\partial x} + \frac{\partial u}{\partial z} \right)^2 \right] dx \right] dz \end{aligned} \quad (59)$$

where l is the length of the overlap. Using the principle of minimum potential energy, the displacements u and w must satisfy the following equations when the adhesive is under static equilibrium.

$$\frac{\partial U}{\partial A_m} = \int \bar{X} u_m dS \quad m=1, 2, 3, K \quad (60)$$

$$\frac{\partial U}{\partial B_m} = \int \bar{Z} w_m dS \quad m=1, 2, 3, K \quad (61)$$

where \bar{X} and \bar{Z} represent the surface loads in x and z directions applied on the adhesive, respectively, and dS covers the periphery of the adhesive. Because the adhesive has two free surfaces at the edges of the overlap, both surface loads \bar{X} and \bar{Z} at the two edges of the overlap

are zero. As described in equations 49 and 50, u_m and w_m are zero at both the upper and lower adhered/adhesive interfaces in order to satisfy the continuity conditions. Therefore, equations 60 and 61 become

$$\frac{\partial U}{\partial A_m} = 0 \quad m = 1, 2, 3, K \quad (62)$$

$$\frac{\partial U}{\partial B_m} = 0 \quad m = 1, 2, 3, K \quad (63)$$

2.2.3 Overall Governing Equations.

Six second-order ordinary differential equations based on equations 43 through 48 and $2n$ algebraic equations from equations 62 and 63 can be obtained with six unknown functions $u^{OU}(x)$, $\psi^U(x)$, $w^U(x)$, $u^{OL}(x)$, $\psi^L(x)$, $w^L(x)$, and $2n$ unknown parameters A_m , B_m , $m = 1, 2, 3, \dots n$ for each of the three regions as defined in figure 16. A total of 36 boundary conditions are needed to solve the 18 second-order ordinary differential equations. These boundary conditions are based on either continuity, applied force, or free surface conditions. A complete list of the boundary conditions is provided in appendix A.

2.2.4 Solution Procedure.

Solutions were obtained by using the symbolic solver, Maple V [39], with the Laplace option. Once the Laplace option is chosen, Maple V performs forward and inverse Laplace transformations to obtain the exact solutions to the system of ordinary differential equations. Twelve initial conditions (values for u^{OU} , ψ^U , w^U , u^{OL} , ψ^L , w^L and their first-order derivatives) at the left end of each of the three regions, $x_1 = 0$, $x_2 = 0$, and $x_3 = 0$, were assumed symbolically to start the solution procedure. These 36 initial conditions were solved together with the 18 unknown coefficients $A = s$ and $B = s$ ($m = 1, 2, 3$) based on the 36 boundary conditions and the equations obtained from equations 62 and 63.

2.3 RESULTS AND DISCUSSION.

2.3.1 Comparison With Finite Element Model.

In order to verify the developed model for stress distribution, finite element analysis using ABAQUS [10 and 11] was conducted following ASTM D 3165-95 specimen configuration with the following dimensions, where the symbols are defined in figure 16.

$$L_1 = L_3 = 80 \text{ mm} \quad L_2 = 30 \text{ mm} \quad \eta = 1 \text{ mm}$$

T300/5208 (Graphite/Epoxy) unidirectional prepreg with a ply thickness of 0.25 mm was used for both upper and lower adherends, each of which consists 12 plies with orientation and sequence $[0_4/90_2]_S$. The engineering constants of T300/5208 are [40]

$$E_x = 181 \text{ GPa} \quad E_y = 10.3 \text{ GPa} \quad G_{xy} = 7.17 \text{ GPa} \quad \nu_{xy} = 0.28$$

Based on the transversely isotropic properties of unidirectional prepreg on the y - z plane, it is common to assume that $E_z = E_y$, $G_{xz} = G_{xy}$, $\nu_{xz} = \nu_{xy}$, and $G_{yz} = E_y/2(1 + \nu_{yz})$ [41]. With the assumed value of 0.35 for ν_{yz} , G_{yz} is calculated as 3.815 GPa. The mechanical constants of the adherends used in the developed model were calculated from the above material properties. Their values per unit width are

$$\begin{array}{ll} A_{11}^U = A_{11}^L = 374 & \text{kN/mm} \\ D_{11}^U = D_{11}^L = 394 & \text{kN mm} \end{array} \quad \begin{array}{ll} B_{11}^U = B_{11}^L = 0 & \text{kN} \\ A_{55}^U = A_{55}^L = 18.2 & \text{kN/mm} \end{array}$$

The choice of the shear correction factor k for anisotropic plates is not trivial. The value of the factor has been shown to depend on both laminate materials and stacking sequence. Some mathematical expressions for shear correction factor have also been provided (Chow [42], Whitney [43], Whitney [44], Bert [45], and Dharmarajan and McCutchen [46]). A value of 5/6 was suggested by Whitney and Pagano [47], and the results were shown to be close to the exact solutions on the cross-ply laminate under bending. In this investigation, a value of 5/6 was chosen for k .

A tensile load of 1,000 N/m was applied at the ends of the joint. The adhesive material was Metlbond 408 with the properties [48]

$$E = 0.96 \text{ GPa} \quad G = 0.34 \text{ GPa} \quad \nu = 0.41$$

Eight-node plane-strain solid elasticity elements with linear stress field were used in the finite element analysis. In order to include the adhesive stress variation through the bondline thickness, eight elements were used to model the adhesive through the thickness.

Figures 18 and 19 show the adhesive shear stress and peel stress (z direction normal stress), respectively, within Region 2 based on both the developed model and the finite element model. As expected, the stress distributions in the upper adherend/adhesive interface are asymmetric from left to right while the stress distributions in the mid plane of the adhesive are symmetric. The maximum adhesive peel and shear stresses occur at the adhesive/adherend corners, i.e., the upper-left and lower-right corners of the adhesive in figure 16. Although certain deviation exists between the developed model and finite element model in the area near the overlap edges, they do present the similar trend. Based on the theory of linearly elasticity, adhesive stresses at the above mentioned corners should be singular. Therefore, it is difficult for linear finite element model to accurately simulate the stresses. The results strongly depend on the element size of finite element model. The finer the mesh is used, the greater the stresses will be calculated around the corners. On the other hand, in the vicinity of the overlap edges where material discontinuity occurs, the force boundary conditions on the adhesive cannot be satisfied exactly. The stresses determined from the developed model are certainly no longer accurate as a result of first-order laminated plate theory. It can be concluded that material yielding must occur near the adhesive/adherend corners. The material nonlinear behavior needs to be considered to determine the precise adhesive stresses. The adhesive stresses obtained from either the developed model or finite element model are not reliable at the singular locations mentioned above. Even so, the stress distributions in the area other than the edges are reliable and were used for failure analysis.

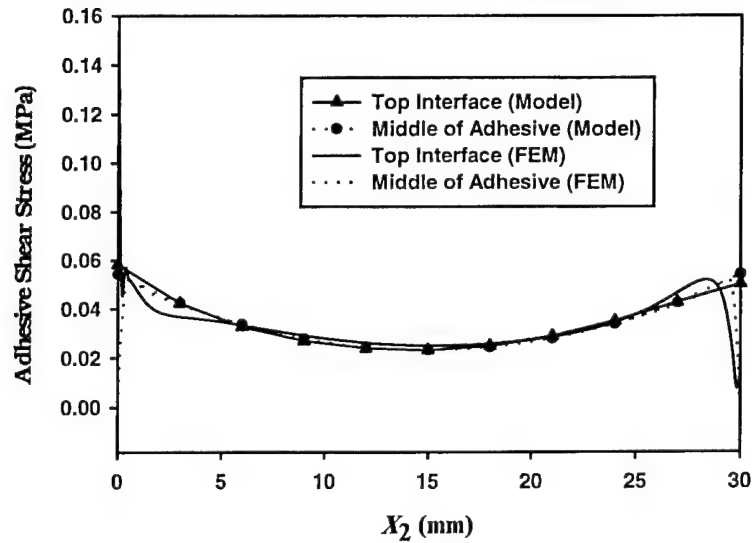


FIGURE 18. ADHESIVE SHEAR STRESS DISTRIBUTION

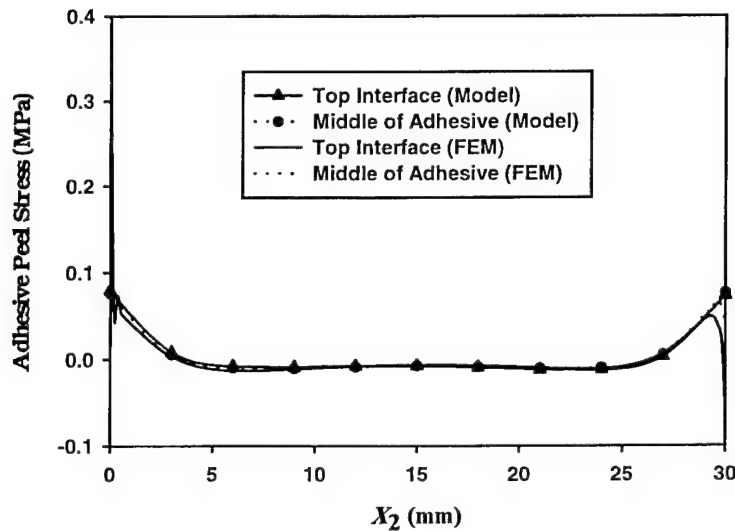


FIGURE 19. ADHESIVE PEEL STRESS DISTRIBUTION

2.3.2 Failure Load Prediction.

The three major failure modes of adhesive-bonded joints are (1) cohesive failure, (2) adhesive failure, and (3) adherend failure. While the first and second modes occur in most of the joints with metallic adherends, the third failure mode is the most common failure mode of bonded joints with composite laminates. Due to the assumption of linear elastic adhesive and adherend, it is appropriate to apply the developed model to analyze the adherend failure mode. In the current investigation, the adherend failure was analyzed with the developed model using first-ply failure criteria.

ASTM D3165 specimen specification was used for both the analytical model and experimental evaluation. Two composite laminates were used as adherends: (1) 1.73-mm-thick FiberCote E765/7781 E-glass/epoxy [0/60/-60/0/-60/60/0] 7-ply satin weave quasi-isotropic laminate and (2) 1.73-mm-thick FiberCote E765/T300 3KPW graphite/epoxy [0/60/-60/0/-60/60/0] 7-ply plain weave quasi-isotropic laminate.

The lamina mechanical properties of both FiberCote E765/7781 glass/epoxy and E765/T300 3KPW graphite/epoxy were experimentally determined at the National Institute for Aviation Research, Wichita State University. The engineering constants of E765/7781 glass/epoxy composites are

$$E_{11} = 26.4 \text{ GPa} \quad E_{22} = 23.6 \text{ GPa} \quad G_{12} = 4.14 \text{ GPa} \quad \nu_{12} = 0.17$$

and the engineering constants of E765/T300 3KPW graphite/epoxy composites are

$$E_{11} = 56.5 \text{ GPa} \quad E_{22} = 55.2 \text{ GPa} \quad G_{12} = 3.86 \text{ GPa} \quad \nu_{12} = 0.076$$

Hysol EA 9394 paste adhesive was used to fabricate the joint specimens. The bulk shear modulus of Hysol EA 9394 was provided by the manufacturer as 1.46 GPa, and the Young's modulus was calculated based on the bulk shear modulus and the assumed Poisson's ratio of 0.45. Therefore, the properties of Hysol EA 9394 used in the model are

$$E = 4.24 \text{ GPa} \quad G = 1.46 \text{ GPa} \quad \nu = 0.45$$

In the present work, four failure criteria were used to evaluate the joint strength: (a) Tsai-Hill failure criterion, (b) von Mises failure criterion, (c) maximum interlaminar tensile stress (z direction) criterion, and (d) maximum normal stress (x direction) criterion.

a. Tsai-Hill Failure Criterion

Tsai-Hill failure criterion can be written as

$$\frac{\sigma_x(\sigma_x - \sigma_z)}{X^2} + \frac{\sigma_z^2}{Z^2} + \frac{\tau_{xz}^2}{R^2} = 1 \quad (64)$$

where σ_x , σ_z , and τ_{xz} are the normal and shear stresses and X , Z , and R are the axial and shear strengths of the adherend lamina. In order to obtain the three parameters X , Z , and R in the failure criterion, nonlinear regression was executed based on data points of each bondline thickness group. For instance, figure 20 shows the predicted joint strength and test data versus bondline thickness based on the parameters obtained from the data group of bondline thickness of approximately 0.35 mm. The critical location of adherend failure was at the adherend adjacent to the upper-left corner of the adhesive bond. Figures 21-23 are the predicted joint strength based on other data groups of bondline thickness as shown in the dashed ovals. As can be seen in figures 20-23, Tsai-Hill criterion does not reflect the trend. As mentioned previously, the adhesive and adherend stresses at the critical corners of the joint are singular. Neither finite element model nor analytical model can provide accurate stress values.

If the location for evaluating failure is moved by 2% of L_2 from the edges of the joints, Tsai-Hill criterion better predicts the failure load as shown in figures 24-27. Similar to figures 24-27 where glass/epoxy adherends were used, figures 28-31 show the predicted joint strengths and test results with graphite/epoxy adherends. However, since the data points in each group were very close for both bondline thickness and failure load, the material inconsistency and measuring errors might have dramatic effects on the regression process in the determination of the three strength parameters X , Z , and R . The determined strength parameters based on each data group and the weight percentage of each term in Tsai-Hill criterion are listed in tables 3-6 for joints with glass/epoxy adherends and tables 7-10 for joints with graphite/epoxy adherends. Apparently, these strength parameters do not compare well with the strength values obtained from laminate coupon tests, and the weight percentage of each term of Tsai-Hill criterion also fluctuates in a large range.

From the composite laminate coupon tests conducted previously at the National Institute for Aviation Research, Wichita State University, the lamina F_1 and F_{13} values, which are 0°-direction tensile and interlaminar shear strengths, respectively, are available for both FiberCote E765/7781 glass/epoxy satin weave and E765/T300 3KPW graphite/epoxy plane weave. These values are $F_1 = 356$ MPa (51.63 ksi), $F_{13} = 63.5$ MPa (9.21 ksi) for E765/7781 glass/epoxy satin weave and $F_1 = 624$ MPa (90.46 ksi), $F_{13} = 71.57$ MPa (10.38 ksi) for E765/T300 3KPW graphite/epoxy plane weave. The F_{13} values were apparent interlaminar shear strengths obtained by short beam shear tests. Because there is no data available for the interlaminar tensile strength for either FiberCote E765/7781 glass/epoxy or E765/T300 3KPW graphite/epoxy, the transverse tensile strength F_2 (42.2 MPa or 6.12 ksi) of E765/T700 24K unitape was used to approximate the interlaminar tensile strength of both FiberCote E765/7781 glass/epoxy satin weave and E765/T300 3KPW graphite/epoxy plane weave under the assumption that the interlaminar tensile strength is dominated by the strength of the resin material. Applying these strength values in Tsai-Hill criterion, i.e., $X = F_1$, $Z = F_2$, and $R = F_{13}$, the curve of failure load vs bondline thickness is provided in figures 32 and 33 for glass/epoxy and graphite/epoxy, respectively. As described previously, the adherend stresses used in figures 32 and 33 for failure analysis were obtained at 2% of L_2 from the edge of the joints. Again, these curves predict the trend well but underestimate the joint strength, especially for thin bondlines.

b. Von Mises Failure Criterion

Von Mises criterion was also used as the failure criterion of the adherend. The expression of von Mises criterion is

$$\left[\sqrt{\sigma_x(\sigma_x - \sigma_z) + \sigma_z^2 + 3\tau_{xz}^2} \right] / S = 1 \quad (65)$$

where S is the von Mises strength.

As was done for Tsai-Hill failure criterion, the S value used in each of the figures 20 through 31, was determined by one data group of a bondline thickness. It can be seen in figures 20 through 31 that no matter which data group is used to generate the strength value S , von Mises criterion can generally predict the strength well with adherend stresses at the edge of the joint and also at 2% of L_2 from the edge.

c. Maximum Interlaminar Tensile Stress (z direction) Criterion

Based on the weight percentages in tables 3-10, the first and second terms of Tsai-Hill criterion are the dominant terms in most cases. Therefore, the interlaminar tensile stress was also considered as the failure criterion of the joint. The criterion, in equation form, is

$$\sigma_z/Z = 1 \quad (66)$$

Again, because there is no available experimental data for interlaminar tensile strength of FiberCote E765/7781 glass/epoxy satin weave and E765/T300 3KPW graphite/epoxy plane weave, the transverse tensile strength (F_2) of E765/T700 24K unitape was used to approximate the interlaminar tensile strength of both FiberCote E765/7781 glass/epoxy satin weave and E765/T300 3KPW graphite/epoxy plane weave. Figures 32 and 33 show the predicted joint strength versus bondline thickness of joints with glass/epoxy and graphite/epoxy adherends, respectively. The stress values used for failure evaluation were obtained at 2% of L_2 from the edge of the joint. Apparently, the maximum interlaminar stress criterion predicts the joint strength better than Tsai-Hill criterion.

d. Maximum Normal Stress (x direction) Criterion

Due to the eccentricity of the load applied to the adherends through the adhesive, the adherends tend to rotate as shown in figure 4. A high tensile stress at the bottom surface of the upper adherend at the edge of the joint is expected. The failed joint specimens also showed that the ply adjacent to the adhesive actually broke at the edge of the overlap and was peeled off from the laminate. These suggest the possibility of applying of the maximum normal stress (in x direction) criterion. The maximum tensile stress failure criterion can be expressed in terms of σ_x and the lamina tensile strength F_1 as

$$\sigma_x/F_1 = 1 \quad (67)$$

Using the experimental strength data (F_1 value) for FiberCote E765/7781 glass/epoxy satin weave and E765/T300 3KPW graphite/epoxy plane weave, the predicted joint strengths are shown in figures 32 and 33. Similarly, the stress values used for failure evaluation were obtained at 2% of L_2 from the edge of the joint. It can be seen that the maximum normal stress criterion correlate fairly well with the experimental data.

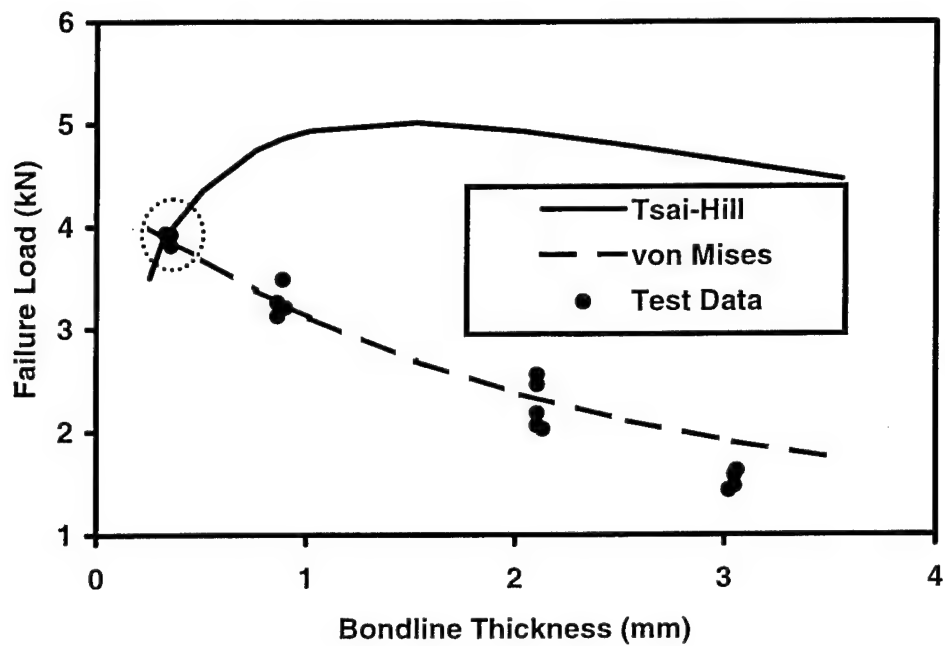


FIGURE 20. STRENGTH PREDICTION OF JOINTS WITH GLASS/EPOXY ADHERENDS BASED ON FIRST DATA GROUP AT $x_2 = 0$

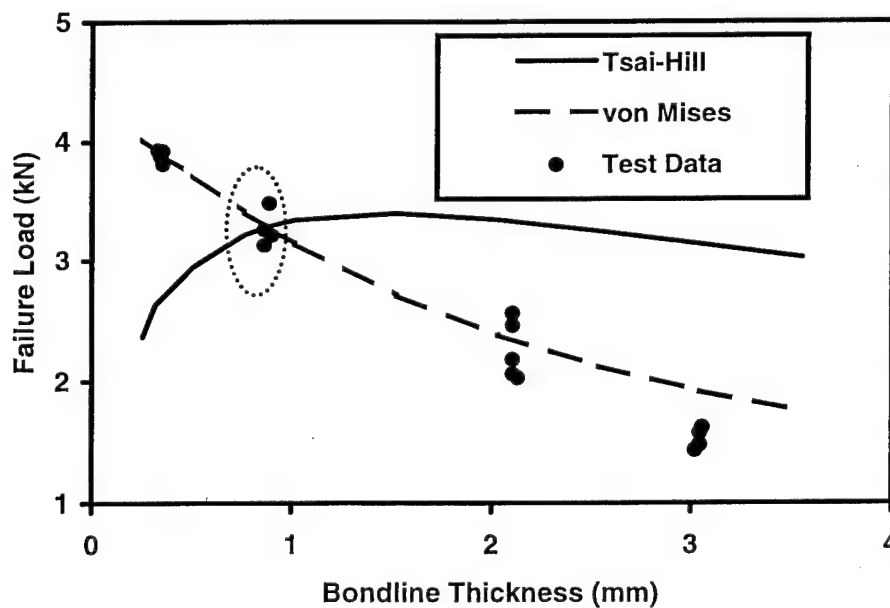


FIGURE 21. STRENGTH PREDICTION OF JOINTS WITH GLASS/EPOXY ADHERENDS BASED ON SECOND DATA GROUP AT $x_2 = 0$

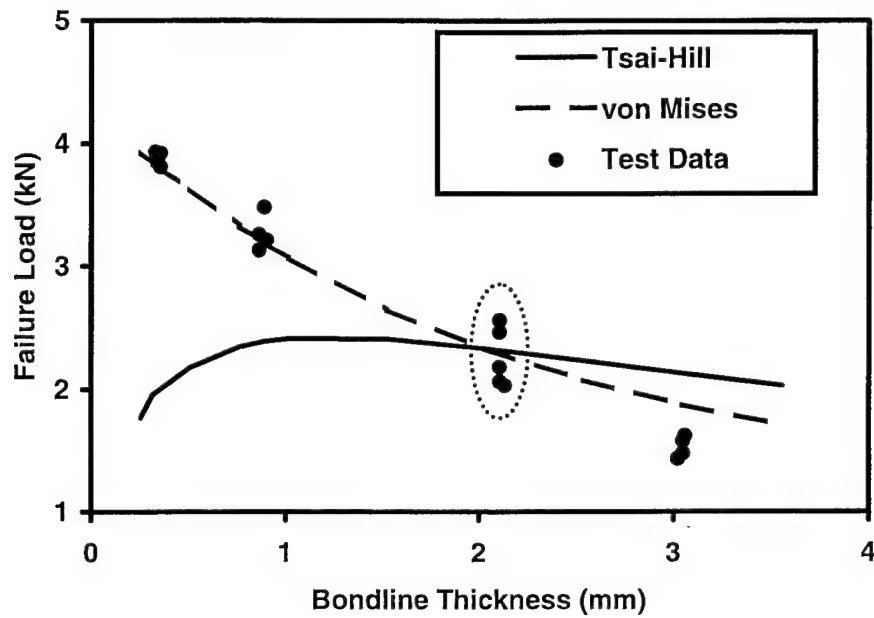


FIGURE 22. STRENGTH PREDICTION OF JOINTS WITH GLASS/EPOXY ADHERENDS BASED ON THIRD DATA GROUP AT $x_2 = 0$

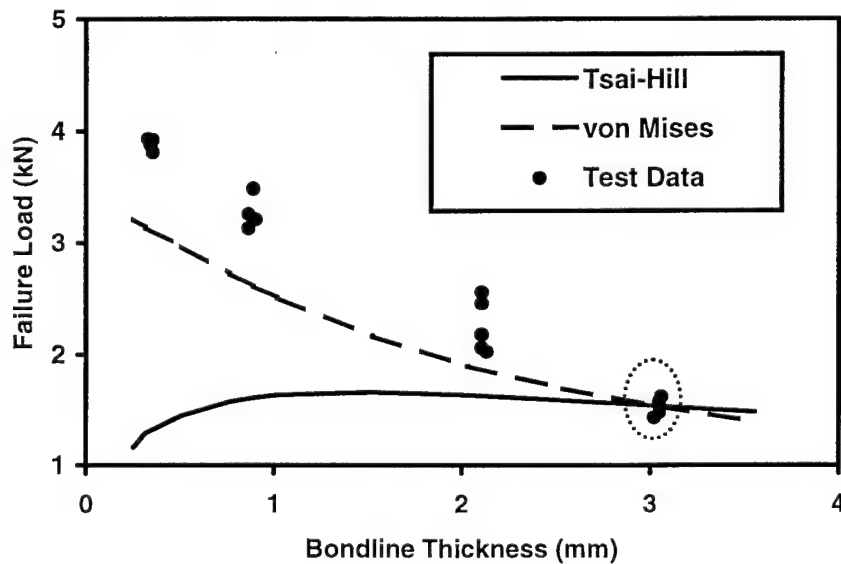


FIGURE 23. STRENGTH PREDICTION OF JOINTS WITH GLASS/EPOXY ADHERENDS BASED ON FOURTH DATA GROUP AT $x_2 = 0$

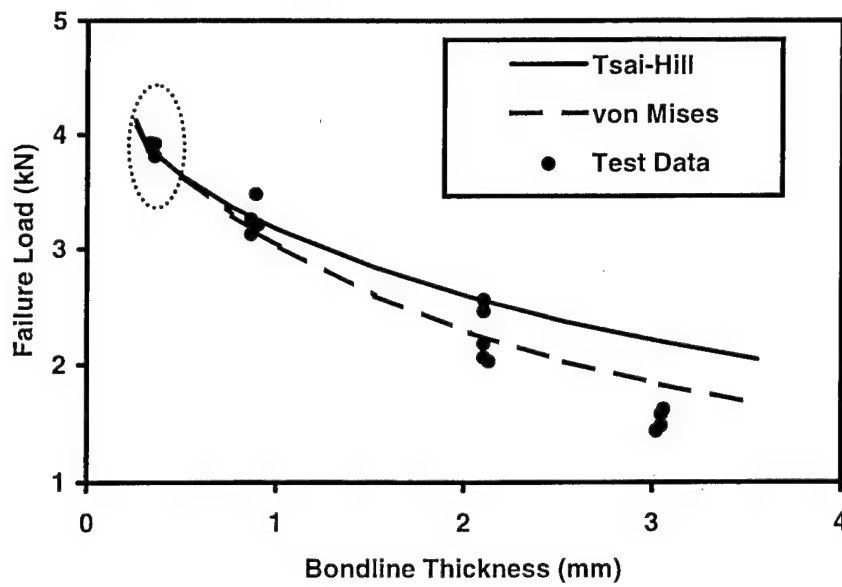


FIGURE 24. STRENGTH PREDICTION OF JOINTS WITH GLASS/EPOXY ADHERENDS
BASED ON FIRST DATA GROUP AT $x_2 = 0.02L_2$

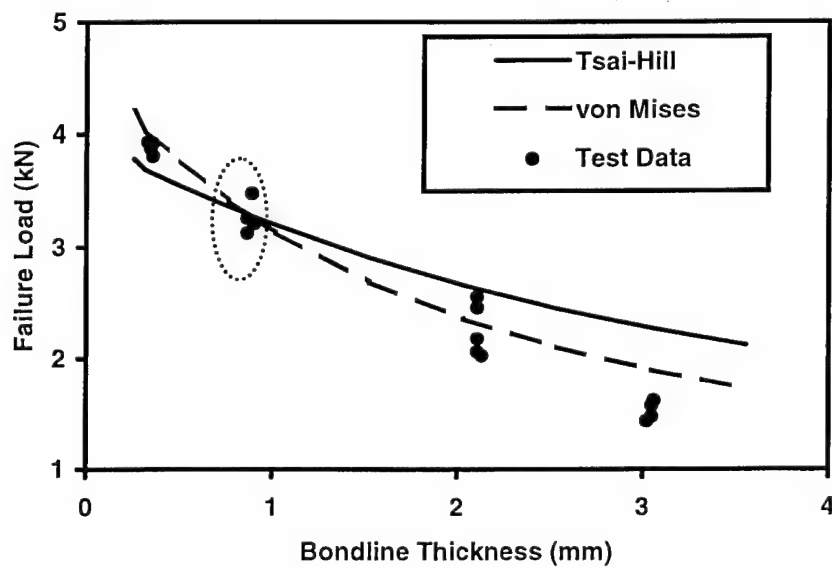


FIGURE 25. STRENGTH PREDICTION OF JOINTS WITH GLASS/EPOXY ADHERENDS
BASED ON SECOND DATA GROUP AT $x_2 = 0.02L_2$

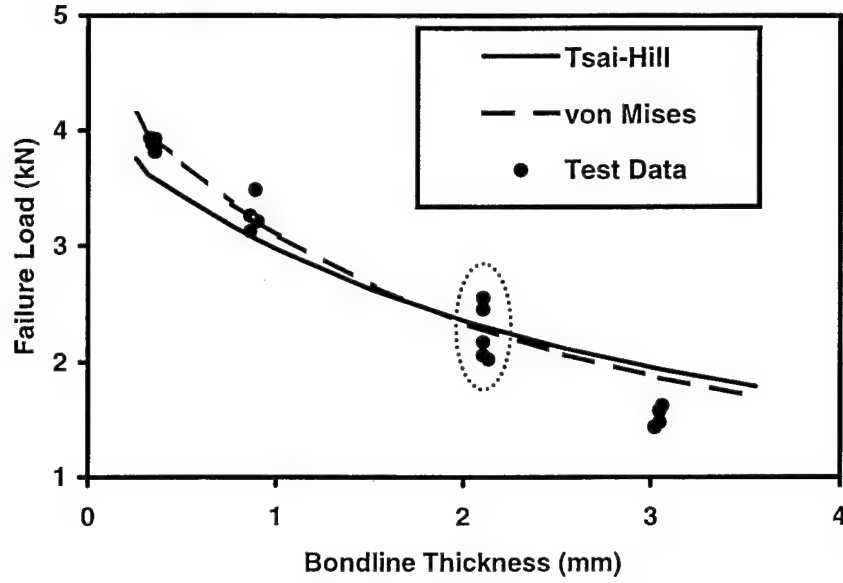


FIGURE 26. STRENGTH PREDICTION OF JOINTS WITH GLASS/EPOXY ADHERENDS
BASED ON THIRD DATA GROUP AT $x_2 = 0.02L_2$

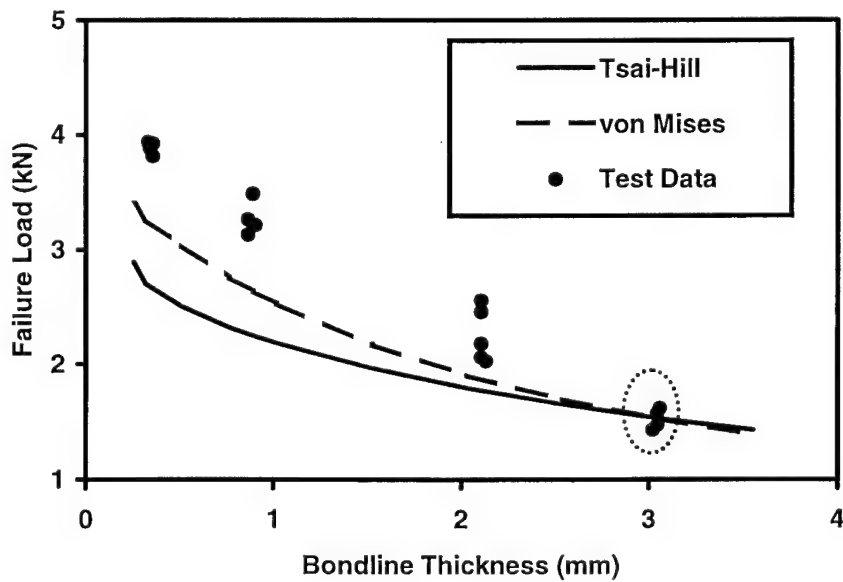


FIGURE 27. STRENGTH PREDICTION OF JOINTS WITH GLASS/EPOXY ADHERENDS
BASED ON FOURTH DATA GROUP AT $x_2 = 0.02L_2$

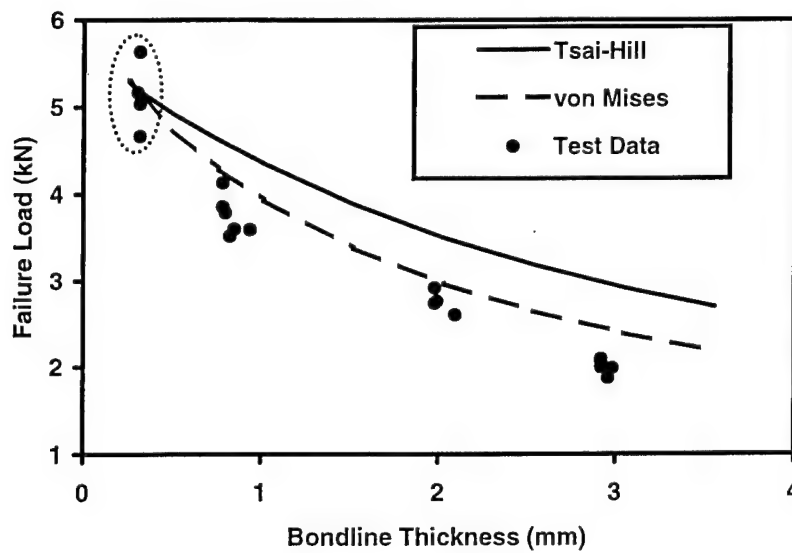


FIGURE 28. STRENGTH PREDICTION OF JOINTS WITH GRAPHITE/EPOXY ADHERENDS BASED ON FIRST DATA GROUP AT $x_2 = 0.02L_2$

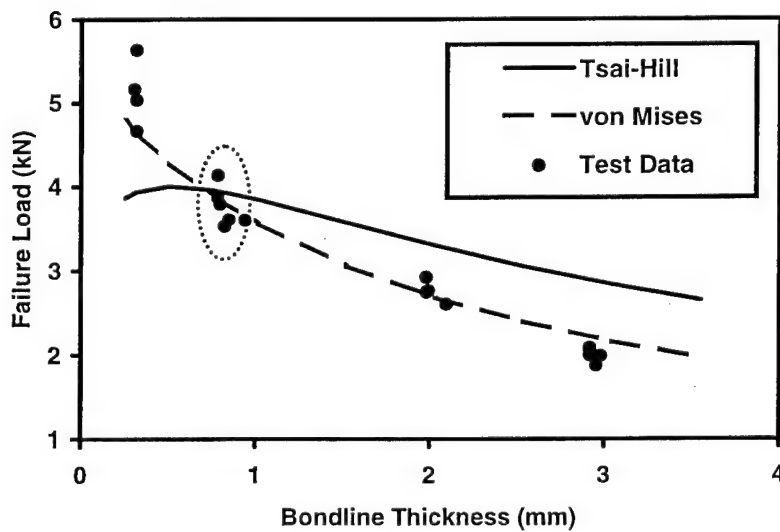


FIGURE 29. STRENGTH PREDICTION OF JOINTS WITH GRAPHITE/EPOXY ADHERENDS BASED ON SECOND DATA GROUP AT $x_2 = 0.02L_2$

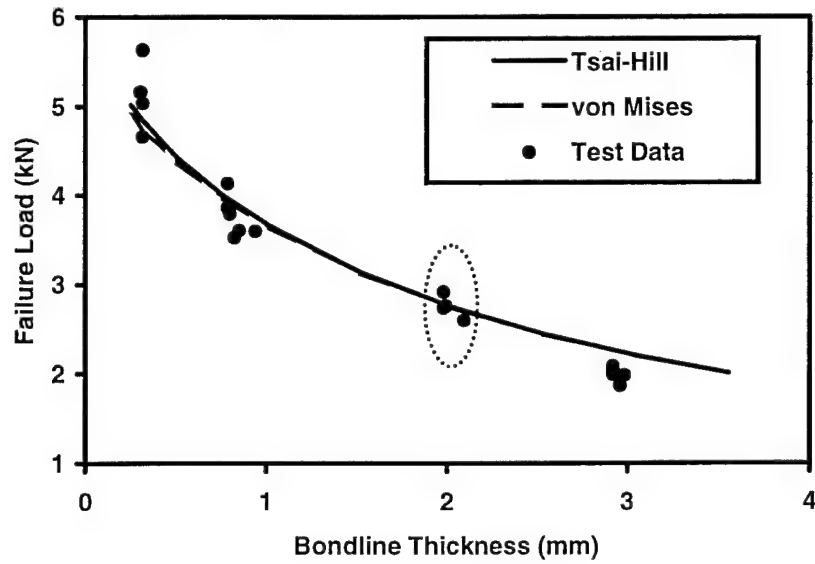


FIGURE 30. STRENGTH PREDICTION OF JOINTS WITH GRAPHITE/EPOXY ADHERENDS BASED ON THIRD DATA GROUP AT $x_2 = 0.02L_2$

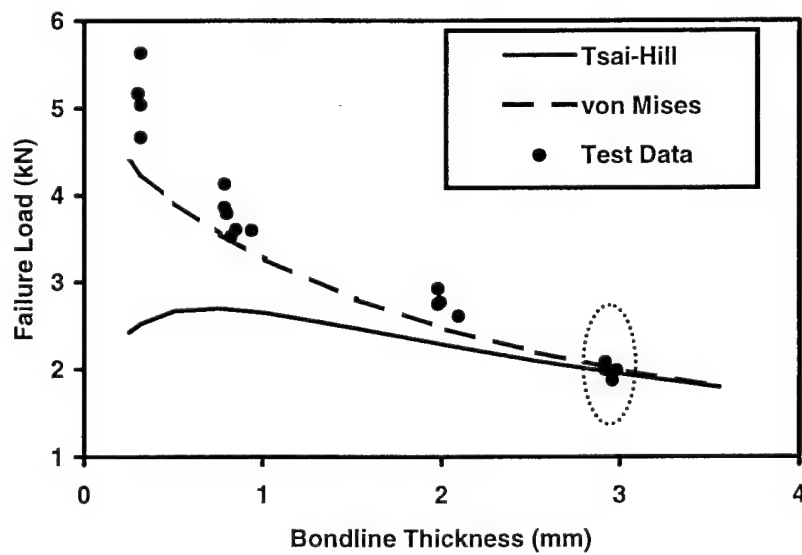


FIGURE 31. STRENGTH PREDICTION OF JOINTS WITH GRAPHITE/EPOXY ADHERENDS BASED ON FOURTH DATA GROUP AT $x_2 = 0.02L_2$

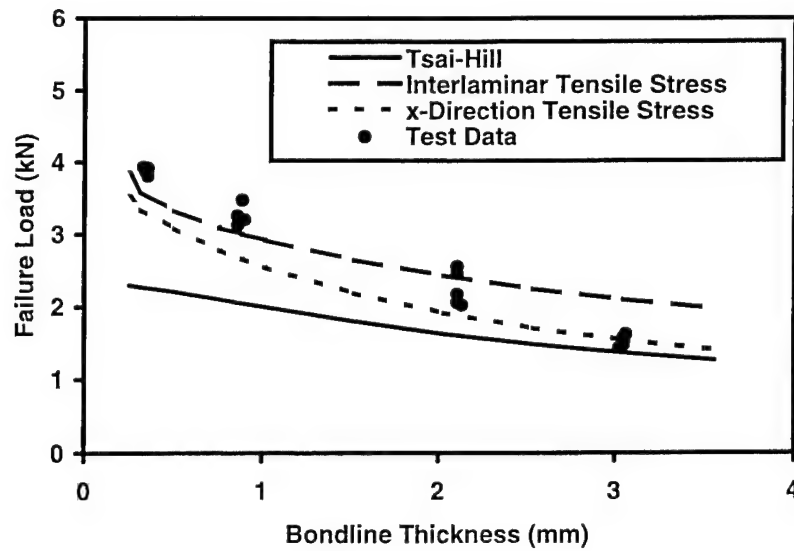


FIGURE 32. STRENGTH PREDICTION OF JOINTS WITH GLASS/EPOXY ADHERENDS BASED ON STRENGTH VALUES FROM COUPON TESTS

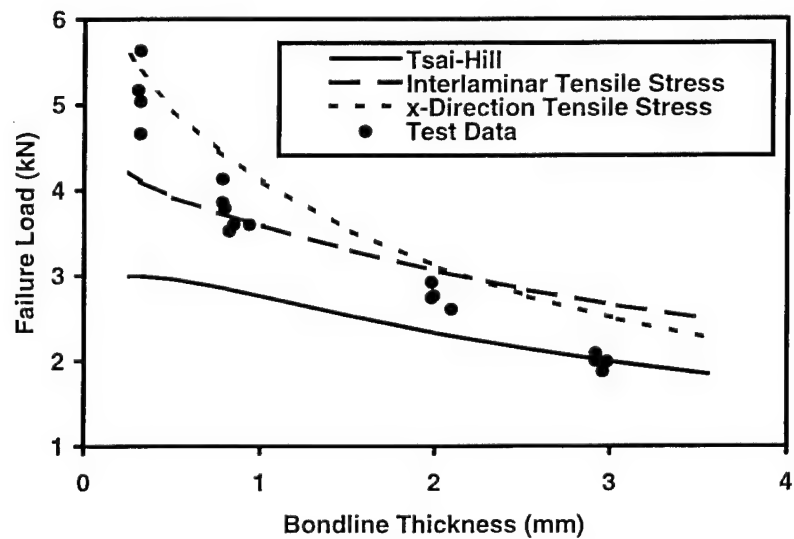


FIGURE 33. STRENGTH PREDICTION OF JOINTS WITH GRAPHITE/EPOXY ADHERENDS BASED ON STRENGTH VALUES FROM COUPON TESTS

TABLE 3. PERCENTAGE OF EACH TERM IN TSAI-HILL CRITERION AND STRENGTH PARAMETERS BASED ON FIRST DATA GROUP WITH GLASS/EPOXY ADHERENDS

Adhesive Thickness	$\sigma_x(\sigma_x - \sigma_z)/X^2$	σ_z^2/Z^2	τ_{xz}^2/R^2
0.30 mm (0.012 in)	14.2%	79.2%	6.6%
0.76 mm (0.03 in)	15.4%	79.8%	4.8%
2.03 mm (0.08 in)	19.4%	76.2%	4.4%
3.05 mm (0.12 in)	21.9%	73.6%	4.5%
Parameters	$X = 1,036 \text{ MPa}$ (150.3 ksi)	$Z = 51.37 \text{ MPa}$ (7.45 ksi)	$R = 295.4 \text{ MPa}$ (42.85 ksi)

TABLE 4. PERCENTAGE OF EACH TERM IN TSAI-HILL CRITERION AND STRENGTH PARAMETERS BASED ON SECOND DATA GROUP WITH GLASS/EPOXY ADHERENDS

Adhesive Thickness	$\sigma_x(\sigma_x - \sigma_z)/X^2$	σ_z^2/Z^2	τ_{xz}^2/R^2
0.30 mm (0.012 in)	2.79E-7%	62.2%	37.8%
0.76 mm (0.03 in)	3.36E-7%	69.7%	30.3%
2.03 mm (0.08 in)	4.51E-7%	70.6%	29.4%
3.05 mm (0.12 in)	5.13E-7%	69.0%	31.0%
Parameters	$X = 7,007 \text{ GPa}$ (1,016 Msi)	$Z = 54.95 \text{ MPa}$ (7.97 ksi)	$R = 117.28 \text{ MPa}$ (17.01 ksi)

TABLE 5. PERCENTAGE OF EACH TERM IN TSAI-HILL CRITERION AND STRENGTH PARAMETERS BASED ON THIRD DATA GROUP WITH GLASS/EPOXY ADHERENDS

Adhesive Thickness	$\sigma_x(\sigma_x - \sigma_z)/X^2$	σ_z^2/Z^2	τ_{xz}^2/R^2
0.30 mm (0.012 in)	38.7%	43.0%	18.3%
0.76 mm (0.03 in)	42.1%	42.6%	15.3%
2.03 mm (0.08 in)	48.3%	38.1%	13.6%
3.05 mm (0.12 in)	51.6%	35.0%	13.4%
Parameters	$X = 597.5 \text{ MPa}$ (86.66 ksi)	$Z = 65.98 \text{ MPa}$ (9.57 ksi)	$R = 152.3 \text{ MPa}$ (22.09 ksi)

TABLE 6. PERCENTAGE OF EACH TERM IN TSAI-HILL CRITERION AND STRENGTH PARAMETERS BASED ON FOURTH DATA GROUP WITH GLASS/EPOXY ADHERENDS

Adhesive Thickness	$\sigma_x(\sigma_x - \sigma_z)/X^2$	σ_z^2/Z^2	τ_{xz}^2/R^2
0.30 mm (0.012 in)	9.7%	90.2%	0.1%
0.76 mm (0.03 in)	10.3%	89.6%	0.1%
2.03 mm (0.08 in)	13.2%	86.7%	0.1%
3.05 mm (0.12 in)	15.1%	84.9%	0.1%
Parameters	$X = 872.1 \text{ MPa}$ (126.5 ksi)	$Z = 33.44 \text{ MPa}$ (4.85 ksi)	$R = 1783 \text{ MPa}$ (258.6 ksi)

TABLE 7. PERCENTAGE OF EACH TERM IN TSAI-HILL CRITERION AND STRENGTH PARAMETERS BASED ON FIRST DATA GROUP WITH GRAPHITE/EPOXY ADHERENDS

Adhesive Thickness	$\sigma_x(\sigma_x - \sigma_z)/X^2$	σ_z^2/Z^2	τ_{xz}^2/R^2
0.30 mm (0.012 in)	34.1%	54.2%	11.7%
0.76 mm (0.03 in)	39.9%	52.1%	8.0%
2.03 mm (0.08 in)	48.5%	45.2%	6.3%
3.05 mm (0.12 in)	52.5%	41.6%	5.9%
Parameters	$X = 981.1 \text{ MPa}$ (142.3 ksi)	$Z = 72.33 \text{ MPa}$ (10.49 ksi)	$R = 224.5 \text{ MPa}$ (32.56 ksi)

TABLE 8. PERCENTAGE OF EACH TERM IN TSAI-HILL CRITERION AND STRENGTH PARAMETERS BASED ON SECOND DATA GROUP WITH GRAPHITE/EPOXY ADHERENDS

Adhesive Thickness	$\sigma_x(\sigma_x - \sigma_z)/X^2$	σ_z^2/Z^2	τ_{xz}^2/R^2
0.30 mm (0.012 in)	1.0%	36.4%	62.6%
0.76 mm (0.03 in)	1.4%	44.5%	54.1%
2.03 mm (0.08 in)	2.1%	46.6%	51.3%
3.05 mm (0.12 in)	2.4%	45.7%	51.9%
Parameters	$X = 4,449 \text{ MPa}$ (645.2 ksi)	$Z = 66.95 \text{ MPa}$ (9.71 ksi)	$R = 74.12 \text{ MPa}$ (10.75 ksi)

TABLE 9. PERCENTAGE OF EACH TERM IN TSAI-HILL CRITERION AND STRENGTH PARAMETERS BASED ON THIRD DATA GROUP WITH GRAPHITE/EPOXY ADHERENDS

Adhesive Thickness	$\sigma_x(\sigma_x - \sigma_z)/X^2$	σ_z^2/Z^2	τ_{xz}^2/R^2
0.30 mm (0.012 in)	99.7%	0.3%	1.63E-8
0.76 mm (0.03 in)	99.8%	0.2%	9.50E-8
2.03 mm (0.08 in)	99.8%	0.2%	6.12E-9
3.05 mm (0.12 in)	99.9%	0.1%	5.38E-9
Parameters	$X = 536.9 \text{ MPa}$ (77.87 ksi)	$Z = 948.8 \text{ MPa}$ (137.6 ksi)	$R = 563.7 \text{ GPa}$ (81,760 ksi)

TABLE 10. PERCENTAGE OF EACH TERM IN TSAI-HILL CRITERION AND STRENGTH PARAMETERS BASED ON FOURTH DATA GROUP WITH GRAPHITE/EPOXY ADHERENDS

Adhesive Thickness	$\sigma_x(\sigma_x - \sigma_z)/X^2$	σ_z^2/Z^2	τ_{xz}^2/R^2
0.30 mm (0.012 in)	3.3%	2.69E-9%	96.7%
0.76 mm (0.03 in)	5.5%	3.71E-9%	94.5%
2.03 mm (0.08 in)	8.3%	3.99E-9%	91.7%
3.05 mm (0.12 in)	9.3%	3.82E-9%	90.7%
Parameters	$X = 1,539 \text{ MPa}$ (223.2 ksi)	$Z = 4,986 \text{ GPa}$ (723.1 Msi)	$R = 37.99 \text{ MPa}$ (5.51 ksi)

3. CONCLUSION.

In this study, finite element analyses were conducted to model the mechanical behavior of adhesive bonded joints configured per ASTM D 5656 specification "Standard Test Method for Thick-Adherend Metal Lap-Shear Joints for Determination of the Stress-Strain Behavior of Adhesives in Shear by Tension Loading." Based on the results of finite element analyses, appreciable error will result from the ASTM D 5656 measuring and data analysis procedures if no adjustments are made. Correction factors are provided to recover the shear modulus of the adhesive being tested. An optimal adhesive thickness of the test specimen as well as a different mounting method for KGR-1 device are proposed to eliminate part of the error. A four-pin arrangement for mounting KGR-1 device, which can eliminate the need for two correction factors in the data analysis, was investigated and is highly recommended for ASTM D 5656 tests. The investigation was limited to linear response of both material and geometry; failure or yield behavior of the adhesive was not studied.

An analytical model was developed to predict the stress distributions of adhesive-bonded composite single-lap joints under tension. The stress variations through the bondline thickness

were included in the model. The results from the developed model correlated well with finite element model (FEM) analysis except in the vicinity of joint edges where mathematical singularities exist.

Based on the developed model, the failure load of adhesive-bonded joints configured according to ASTM D3165 specimen specification was predicted using four failure criteria of the composite adherend: Tsai-Hill failure criterion, von Mises failure criterion, maximum interlaminar tensile stress criterion, and maximum x direction tensile stress criterion. The parameters used in Tsai-Hill and von Mises criteria were obtained through nonlinear regression based on the selected joint test data. Once the parameters were determined, failure loads of joints with other geometries were then predicted and compared with test results. When adherend stresses at the adhesive/adherend interface and at a distance of 2% of overlap length from the edge of the joint were used to evaluate failure, both the Tsai-Hill and von Mises criteria provide reasonably good joint strength predictions even though the strength parameters might not be reasonable. Lamina strength values from laminate coupon tests were used for Tsai-Hill, maximum interlaminar tensile stress, and maximum x direction tensile stress criteria. It was shown that the maximum interlaminar tensile stress criterion and the maximum x direction tensile stress criterion predict the joint strength better than Tsai-Hill and von Mises criteria.

The use of a 2% of the overlap length offset from the edge of the joint for failure evaluation was shown to be effective on the standard ASTM D 3165 specimen geometry. Further experiments with various overlap lengths are needed to validate the use of the 2% offset.

4. REFERENCES.

1. Kutscha, D., "Mechanics of Adhesive-Bonded Lap-Type Joints: Survey and Review," Technical Report AFML-TDR-64-298, 1964.
2. Kutscha, D. and Hofer, K. E. Jr., "Feasibility of Joining Advanced Composite Flight Vehicles," Technical Report AFML-TR-68-391, 1969.
3. Kreiger, R.B., "Stiffness Characteristics of Structural Adhesives for Stress Analysis in Hostile Environment," American Cyanamid Company, 1975.
4. Krieger, R. B. Jr., "Stress Analysis Concepts for Adhesive Bonding of Aircraft Primary Structure," Adhesively Bonded Joints: Testing, Analysis, and Design, ASTM STP 981, W. S. Johnson, ed., American Society for Testing and Materials, Philadelphia, PA, pp. 264-275, 1988.
5. Hughes, E. J. and Krieger, R. B. Jr., "Mechanical Properties of Adhesives," Materials Engineering, Adhesive Bonding of Aluminum Alloys, E. W. Thrall, R. W. Shannon eds., pp. 141-175, 1986.
6. Krieger, R. B. Jr., "Analyzing Joint Stresses Using an Extensometer," *Adhesives Ages*, pp. 26-28, 1985.

7. Krieger, R. B. Jr., "Stress Analysis Concepts for Adhesive Bonding of Aircraft Primary Structure," International Conference on Structural Adhesives in Engineering, Bristol, England, pp. 1-10, 1986.
8. Tsai, M.Y., Morton, J., Krieger, R.B., and Oplinger, D.W., "Experimental Investigation of the Thick-Adherend Lap Shear Test," *Journal of Advanced Materials*, V. 27, No. 3, pp. 28-36, 1996.
9. Kassapoglou, C. and Adelman, J. C., "KGR-1 Thick Adherend Specimen Evaluation for the Determination of Adhesive Mechanical Properties," Proceedings 23rd International SAMPE Technical Conference, October 21 - 24, 1991.
10. *ABAQUS/CAE User's Manual*, Version 2, Hibbitt, Karlsson & Sorensen, Inc., 1999.
11. *ABAQUS Theory Manual*, Version 5.8, Hibbitt, Karlsson & Sorensen, Inc., 1998.
12. Matthews, F. L., Kilty, P. F., and Goodwin, E. W., "A Review of the Strength of Joints in Fibre-Reinforced Plastics: Part 2 Adhesively Bonded Joints," *Composites*, pp. 29-37, 1982.
13. Vinson, J. R., "Adhesive Bonding of Polymer Composites," *Polymer Engineering and Science*, Vol. 29, pp. 1325-1331, 1989.
14. Goland, M. and Reissner, E., "The Stresses in Cemented Joints," *Journal of Applied Mechanics*, Vol. 11, pp. A-17-A-27, 1944.
15. Hart-Smith, L. J., "Adhesive-Bonded Single-Lap Joints," Douglas Aircraft Co., NASA Langley Report CR 112236, 1973.
16. Hart-Smith, L. J., "Adhesive-Bonded Double-Lap Joints," Douglas Aircraft Co., NASA Langley Report CR 112235, 1973.
17. Hart-Smith, L. J., "Adhesive-Bonded Scarf and Stepped-Lap Joints," Douglas Aircraft Co., NASA Langley Report CR 112237, 1973.
18. Hart-Smith, L. J., "Analysis and Design of Advanced Composite Bonded Joints," Douglas Aircraft Co., NASA Langley Report CR-2218, 1974.
19. Reissner, E., "The Effect of Transverse Shear Deformation on the Bending of Elastic Plates," *Journal of Applied Mechanics*, Vol. 12, A-69-A-77, 1945.
20. Reddy, J. N., "A Refined Nonlinear Theory of Plates With Transverse Shear Deformation," *International Journal of Solids Structures*, Vol. 20, pp. 881-896, 1984.
21. Renton, W. J., and Vinson, J. R., "Analysis of Adhesively Bonded Joints Between Panels of Composite Materials," *Journal of Applied Mechanics*, Vol. 44, pp. 101-106, 1977.

22. Griffin, S. A., Pang, S. S., and Yang, C., "Strength Model of Adhesive Bonded Composite Pipe Joints under Tension," *Polymer Engineering and Science*, Vol. 31, pp. 533-538, 1991.
23. Yang, C., Pang, S. S., and Griffin, S. A., "Failure Analysis of Adhesive-Bonded Double-Lap Joints Under Cantilevered Bending," *Polymer Engineering and Science*, Vol. 32, pp. 632-40, 1992.
24. Yang, C. and Pang, S. S., "Stress-Strain Analysis of Single-Lap Composite Joints Under Cylindrical Bending," *Composites Engineering*, Vol. 3, pp. 1051-1063, 1993.
25. Yang, C. and Pang, S.S., "Stress-Strain Analysis of Single-Lap Composite Joints Under Tension," *ASME Transaction - Journal of Engineering Materials and Technology*, Vol. 118, pp. 247-255, 1996.
26. Oplinger, D. W., "Effects of Adherend Deflections in Single Lap Joints," *International Journal of Solids and Structures*, Vol. 31, pp. 2565-2587, 1994.
27. Tong, L., "An Assessment of Failure Criteria to Predict the Strength of Adhesively Bonded Composite Double Lap Joints," *Journal of Reinforced Plastics and Composites*, Vol. 16, No. 8, pp. 698-713, 1997.
28. Adams, R.D. and Davies, R., "Strength of Joints Involving Composites," *Journal of Adhesion*, Vol. 59, pp. 171-182, 1996.
29. Thomas, R., Garcia, F.J., and Adams, R.D., "Adhesive Joining of Composite Laminates," *Plastics, Rubber, and Composite Processing and Applications*, Vol. 27, No. 4, pp. 200-205, 1998.
30. Chiang, M.Y.M. and Chai, H., "Plastic Deformation Analysis of Cracked Adhesive Bonds Loaded in Shear," *International Journal of Solids Structures*, Vol. 31, No. 18, pp. 2477-2490, 1994.
31. Chai, H. and Chiang, M.Y.M., "A Crack Propagation Criterion Based on Local Shear Strain in Adhesive Bonds Subjected to Shear," *Journal the Mechanics and Physics of Solids*, Vol. 44, No. 10, pp. 1669-1689, 1996.
32. Ju, S.H., Sandor, B.I., and Plesha, M.E., "Life Prediction of Solder Joints by Damage and Fracture Mechanics," *Journal of Electronic Packaging*, Vol. 118, pp. 193-200, 1996.
33. Needleman, A. and Rosakis, A.J., "Effect of Bond Strength and Loading Rate on the Conditions Governing the Attainment of Intersonic Crack Growth Along Interfaces," *Journal of the Mechanics and Physics of Solids*, Vol. 47, No. 12, pp. 2411-2449, 1999.
34. Kinloch, A.J., Wang, Y., Williams, J.G., and Yayla, P., "The Mixed-Mode Delamination of Fibre-Composite Materials," *Composites Science and Technology*, Vol. 47, pp. 225-237, 1993.

35. Charalambides, M.N., Hardouin, R., Kinloch, A.J., and Matthews, F.L., "Adhesively-Bonded Repairs to Fibre Composite Materials I: Experimental," *Composites Part A*, Vol. 29A, pp. 1371-1381, 1998.
36. Charalambides, M.N., Kinloch, A.J., and Matthews, F.L., "Adhesively-Bonded Repairs to Fibre-Composite Materials II: Finite Element Modeling," *Composites Part A*, Vol. 29A, pp. 1383-1396, 1998.
37. Kinloch, A.J., Jethwa, J.K.K., and Osiyemi, S.O., "Fatigue Behaviour of Adhesive Joints," Proceedings of the European Conference on Adhesion, September 12-15, 1994.
38. Jethwa, J.K.K. and Kinloch, A.J., "Fatigue and Durability Behavior of Automotive Adhesives. Part I: Fracture Mechanics Tests," *Journal of Adhesion*, Vol. 61, No. 1-4, pp. 71-95, 1997.
39. Monagan M. B., Geddes, K. O., Heal, K. M., Labahn, G., and Vorkoetter, S. *Maple V Programming Guide*, Springer-Verlag, New York, 1998.
40. Tsai, Stephen W. and Hahn, H. Thomas, *Introduction to Composite Materials*, Technomic Publishing Company, Inc., Lancaster, PA, 1980.
41. Whitney, J. M., *Structural Analysis of Laminated Anisotropic Plates*, Technomic Publishing Company, Inc., Lancaster, PA, 1987.
42. Chow, J. S., "On the Propagation of Flexural Waves in an Orthotropic Plate and its Response to an Impulsive Load," *Journal of Composite Materials*, Vol. 5, pp. 306-319, 1971.
43. Whitney, J. M., "Stress Analysis of Thick Laminated Composite and Sandwich Plates," *Journal of Composite Materials*, Vol. 6, pp. 426-440, July 1972.
44. Whitney, J. M., "Shear Correction Factors for Orthotropic Laminates Under Static Load," *Journal of Applied Mechanics*, Vol. 40, pp. 302-304, 1973.
45. Bert, C. W., "Simplified Analysis of Static Shear Factors for Beams of Nonhomogeneous Cross Section," *Journal of Composite Materials*, Vol. 7, pp. 525-529, 1973.
46. Dharmarajan, S. and McCutchen, H. Jr., "Shear Coefficients for Orthotropic Beams," *Journal of Composite Materials*, Vol. 7, pp. 530-535, 1973.
47. Whitney, J. M. and Pagano, N. J., "Shear Deformation in Heterogeneous Anisotropic Plates," *Journal of Applied Mechanics*, Vol. 37, pp. 1031-1036, 1970.
48. Adams, R.D. and Wake, W.C., *Structural Adhesive Joints in Engineering*, Elsevier Applied Science Publishers, London and New York, 1984.

APPENDIX A—BOUNDARY CONDITIONS FOR CLOSED FORM MODEL

Region 1 At $x_1 = 0$,

$$u_1^{oU} = 0 \quad (A-1)$$

$$w_1^U = 0 \quad (A-2)$$

$$M_{y,1}^U = 0 \quad (A-3)$$

$$u_1^{oL} = 0 \quad (A-4)$$

$$M_{y,1}^L = 0 \quad (A-5)$$

$$Q_{z,1}^L = 0 \quad (A-6)$$

At $x_1 = L_1$ ($x_2 = 0$ in Region 2),

$$u_1^{oU} = u_2^{oU} \quad (A-7)$$

$$\psi_1^U = \psi_2^U \quad (A-8)$$

$$w_1^U = w_2^U \quad (A-9)$$

$$\frac{du_1^{oU}}{dx_1} = \frac{du_2^{oU}}{dx_2} \quad (A-10)$$

$$\frac{d\psi_1^U}{dx_1} = \frac{d\psi_2^U}{dx_2} \quad (A-11)$$

$$\frac{dw_1^U}{dx_1} = \frac{dw_2^U}{dx_2} \quad (A-12)$$

$$N_{x,1}^L = 0 \quad (A-13)$$

$$M_{y,1}^L = 0 \quad (A-14)$$

$$Q_{z,1}^L = 0 \quad (A-15)$$

Region 2 At $x_2 = 0$,

$$N_{x,2}^L = 0 \quad (\text{A-16})$$

$$M_{y,2}^L = 0 \quad (\text{A-17})$$

$$Q_{z,2}^L = 0 \quad (\text{A-18})$$

At $x_2 = L_2$, ($x_3 = 0$ in Region 3),

$$N_{x,2}^U = 0 \quad (\text{A-19})$$

$$M_{y,2}^U = 0 \quad (\text{A-20})$$

$$Q_{z,2}^U = 0 \quad (\text{A-21})$$

$$u_2^{oL} = u_3^{oL} \quad (\text{A-22})$$

$$\psi_2^L = \psi_3^L \quad (\text{A-23})$$

$$w_2^L = w_3^L \quad (\text{A-24})$$

$$\frac{du_2^{oL}}{dx_2} = \frac{du_3^{oL}}{dx_3} \quad (\text{A-25})$$

$$\frac{d\psi_2^L}{dx_2} = \frac{d\psi_3^L}{dx_3} \quad (\text{A-26})$$

$$\frac{dw_2^L}{dx_2} = \frac{dw_3^L}{dx_3} \quad (\text{A-27})$$

Region 3 At $x_3 = 0$,

$$N_{x,3}^U = 0 \quad (\text{A-28})$$

$$M_{y,3}^U = 0 \quad (\text{A-29})$$

$$Q_{z,3}^U = 0 \quad (\text{A-30})$$

$$N_{x,3}^U = \frac{P A_{11}^U}{A_{11}^U + A_{11}^L + E\eta} \quad (\text{A-31})$$

$$M_{y,3}^U = 0 \quad (\text{A-32})$$

$$Q_{z,3}^U = 0 \quad (\text{A-33})$$

$$N_{x,3}^L = \frac{P A_{11}^L}{A_{11}^U + A_{11}^L + E\eta} \quad (\text{A-34})$$

$$M_{y,3}^L = 0 \quad (\text{A-35})$$

$$Q_{z,3}^L = 0 \quad (\text{A-36})$$